



# The Stability of a Dense Crust Situated on Small Bodies

Yoshinori Miyazaki<sup>1</sup> and David J. Stevenson<sup>1</sup>Division of Geological and Planetary Sciences, California Institute of Technology, Pasadena, CA 91125, USA; [ymiya@caltech.edu](mailto:ymiya@caltech.edu)

Received 2023 December 2; revised 2024 July 1; accepted 2024 July 18; published 2024 August 30

## Abstract

Small planetary bodies in the solar system, including Io, Ganymede, and Callisto, may have a crust denser than their underlying mantle. Despite the inherent gravitational instability of such structures, we show that the growth timescale of the Rayleigh–Taylor (RT) instability can be as long as the age of the solar system, owing to the strong temperature dependence of viscosity. Even in cases where the instability timescale is shorter, the instability is confined to a thin layer at the base of the crust, making the foundering of the entire crust improbable in many scenarios. This study delineates the onset and aftermath of the RT instability, applying a quantitative framework to assess the stability of (i) rock-contaminated crust on icy satellites, and (ii) silicate crust floating on top of a subsurface magma ocean on Io. Notably, for Io the RT instability peels off only 10–100 m from the crust’s base, and thermal diffusion rapidly recovers the crustal thickness through solidification of a magma ocean. Despite recurrent delamination of the crustal base, the initial crustal thickness is maintained by thermal diffusion, virtually stabilizing a floating dense crust. Cracking of the crust also is unlikely to result in the foundering of the crust. A dense crust on a small body is therefore difficult to be overturned, suggesting the potential ubiquity of dense surface layers throughout the solar system.

*Unified Astronomy Thesaurus concepts:* Io (2190); Galilean satellites (627); Callisto (2279); Ganymede (2188)

## 1. Introduction

A common illustration of a planetary interior shows a layered structure with denser materials located toward the center. This picture is correct for a wide range of planetary bodies; for Earth, the atmosphere, crust, mantle, and core are in the order of increasing density. Although a clear boundary between layers does not exist under extreme conditions, the same is true for gas giants, including Jupiter and Saturn (Wahl et al. 2017; Mankovich & Fuller 2021). Such a picture, however, may not necessarily be the case for smaller dwarf planets or satellites. Ceres, for example, may have been polluted at the surface by incoming undifferentiated impactors after it had partially differentiated, so that the subsurface is more ice-rich than the bulk composition of the accreted material. Such a scenario may also apply to Ganymede or Callisto, which have crusts covered by “dirty ice” (Shoemaker et al. 1982). The dirty ice that constitutes the darker terrain of Ganymede contains a nonnegligible amount of silicate (Spencer 1987), and the crust is thus probably heavier than the underlying clean ice and the much deeper liquid water ocean.<sup>1</sup>

A dense crust, which is heavier than the underlying mantle, could also be present on Io. The reanalysis of Galileo magnetometer data has suggested the existence of a highly molten layer in the subsurface that has a melt fraction of 0.2 or

higher (Khurana et al. 2011). This could be a magma ocean, possibly with suspended crystals, which is rheologically very different from a partial melt (Miyazaki & Stevenson 2022). Because the solid phase is denser than the liquid phase for silicates of the same composition, such a subsurface liquid layer, unlike ice, implies a density inversion at the crust–mantle boundary. It would indeed be unstable if the composition of the liquid and solid were similar, as expected for the case of extreme melting suggested for Io.

When heavy material sits above a lighter one, the system typically undergoes overturn, commonly known as the Rayleigh–Taylor (RT) instability (e.g., Chandrasekhar 1961). The possible existence of a dense crust in small celestial bodies thus poses the question of how such a structure maintains stability over the long term. While diapiric upwelling due to small-scale RT instability has been explored to explain certain features of small icy bodies (e.g., Shoji & Kurita 2014; Stein et al. 2023), we discuss the onset of the instability to assess the stability of the entire crust in this study. A similar approach has been applied to Kuiper Belt objects, and Rubin et al. (2014) showed that an undifferentiated rock–ice mixture could be situated on top of an icy mantle. Even for Galilean icy satellites, it has been implied in multiple studies that the dense crust may remain stable for billions of years due to its elastic or very viscous nature (e.g., Nagel et al. 2004; McKinnon 2006). In this study, the stability of a dense crust is investigated by employing physical models and analyses.

We simplify the argument by considering a two-layer system with a dense crust and the underlying lighter mantle.<sup>2</sup> In the first part of the paper (Sections 2–4), we estimate the time and

<sup>1</sup> Here and throughout we use the word “crust” rather loosely to mean a surface layer that is different in composition from the underlying material for any reason. On terrestrial bodies such as Earth, “crust” is much more tightly defined to be a compositionally distinct layer arising from petrological processes. It also happens to be colder and often more viscous than the underlying material, but this is a separate attribute. The lithosphere should not be confused with the crust, but unfortunately this is often not made clear for icy satellites, where some of the literature uses the word crust to mean the outer layer of icy bodies, as for the outer ice shell of Europa or Enceladus.

<sup>2</sup> We note that it is strictly a three-layer system: the uppermost layer is free space (zero density), and the intermediate layer (crust) is of specified thickness but higher density than the bottom layer, which is effectively infinite in extent. But only the density difference between the crust and the interior is relevant to the instability under consideration because the topmost surface is assumed to be immobile. This is important since any vertical deformation of the topmost interface is highly stabilizing because of the large density difference relative to free space.



length scales of the RT instability under depth-dependent viscosity. The framework is then applied to discuss how the instability develops on small bodies, including Ganymede, Callisto, and Io. The growth timescale can easily be longer than the age of the solar system for many cases, and even when shorter, we demonstrate that the onset of the instability does not necessarily destabilize the entire crust. The predominant deformation mechanism may not be viscous, especially at low temperatures, so we also discuss whether elasticity can prevent the overturn from happening entirely (Section 4.4). In the later sections, alternative mechanisms beyond the RT instability are considered as a potential overturn mechanism, including fractures (Section 5) and impacts (Section 6), because the finite strength of material influences its rheological behavior under a sufficiently high stress and low temperature. We conclude the paper by discussing how the presence of a dense crust contributes to a small increase in the momentum of inertia.

## 2. The Timescale of the Rayleigh–Taylor Instability

The dispersion relations of the RT instability have been derived for various settings (e.g., Molnar et al. 1998; Kaus & Becker 2007; Terrones & Carrara 2015), yielding insights into many terrestrial phenomena, such as crust delamination (Conrad & Molnar 1997; Mondal & Korenaga 2018) and core formation (Stevenson 1990; Sasaki & Abe 2007). In this section, we consider the stability of a two-layer system, representing a crust and mantle, and investigate its instability timescale.

On timescales of the RT instability, a crustal layer can either be predominantly viscous or elastic (albeit with finite strength) depending on the material properties. The dominant expected behavior, however, can be predicted from the Maxwell timescale, given by

$$\tau_M = \frac{\eta}{\mu}, \quad (1)$$

where  $\eta$  is viscosity and  $\mu$  is shear modulus. The effective viscosity and therefore the Maxwell time of surficial icy crust depends on many parameters, including principal stress level, grain size, and the presence of nonice contaminants, and  $\tau_M$  can easily be as long as the age of the body. The shear modulus is also uncertain, but its uncertainty is much smaller. For example, Figure 6 of Goldsby & Kohlstedt (2001) suggests that the viscosity at a typical Ceres surface temperature (165 K) is less than 10 orders of magnitude larger than the melting point value. Assuming a rheology resembling pure ice, a maximum Maxwell time of a few Myr follows, with  $\eta \leq 10^{23}$  Pa s and  $\mu = 10^9$  Pa. Meanwhile, the typical surface temperature of Ganymede (130 K) corresponds to a Maxwell time that may exceed the age of the body, especially for low stress levels ( $\eta = 10^{26}$  Pa s at a stress of 10 MPa and a grain size of 1 mm). This implies that the near-surface layer of these bodies does not behave viscously for the duration of the RT instability, and, in some cases, even over geologic timescales. Viscosity, however, decreases dramatically with depth due to increasing temperature and could be much lower at the crust–mantle boundary. The rheological behavior thus changes depending on the crustal thickness and its thermal structure, motivating us to consider

both viscous (Section 2.1) and elastic cases (Section 4.4) in the following.

While the two end-members of purely viscous and elastic rheology are considered in this study, we note that ice and silicate are not necessarily Maxwellian (e.g., Shoji et al. 2013), and the role of anelastic response in tidal dissipation has been recognized (Biersen & Nimmo 2016; Keane et al. 2023). The creep response function for the Andrade rheology, which is commonly employed in planetary science, is given by (e.g., McCarthy & Castillo-Rogez 2013)

$$J(t) = \frac{1}{\mu} + \beta t^m + \frac{t}{\eta}, \quad (2)$$

where each term represents elastic (instantaneous), anelastic (transient), and viscous deformations, respectively. The constants  $\beta$  and  $m$  describe the magnitude and time dependence of the anelastic response, and experimental studies suggest values of  $\beta = 10^{-13}$ – $10^{-11}$  Pa<sup>-1</sup> s<sup>-m</sup> and  $m \simeq 0.3$  for both olivine and ice (Jackson et al. 2004; Castillo-Rogez et al. 2011). Although anelasticity influences the magnitude of tidal dissipation (Renaud & Henning 2018), its contribution is mostly negligible in the cases discussed here. For the majority of cases, viscous strain dominates the deformation during the RT instability ( $\tau \gg \tau_M$ ), where the anelastic strain is smaller than the viscous strain ( $\beta \tau^m \ll \tau/\eta$ ) over the discussed timescales ( $\tau = 10^{6-9}$  yr). Meanwhile, anelastic deformation may become important in the elastic end-member scenario, which is relevant to the stability of the cold surficial layer (Section 4.4). Its effect, however, remains uncertain, as the magnitude of anelastic strain under the crustal surface conditions is poorly constrained. Whereas the constant  $\beta$  is expected to be smaller than  $10^{-13}$  at such conditions (Figure 4 of Castillo-Rogez et al. 2011), leading to minimal anelastic effect, further studies are warranted for a more detailed analysis.

### 2.1. Viscous Crust–Mantle Boundary

We first consider a case where viscosity within the upper layer decreases with depth. Temperature within the crust increases with depth, so a substantial decrease in viscosity is expected in the subsurface region. We later consider the case of a thin layer of a constant viscosity, but the consequences are very similar. This is because the viscosity gradient will concentrate the flow into a thin viscosity scale height that is determined by the thermal gradient and the  $T$ -dependence of the rheology.

Viscosity is generally given by

$$\eta = \eta_0 \left( \frac{\sigma}{\sigma_0} \right)^{1-n} \exp \left( \frac{E}{R} \left( \frac{1}{T} - \frac{1}{T_0} \right) \right), \quad (3)$$

where  $n$  is the stress exponent of the flow law,  $E$  is the activation energy,  $R$  is the universal gas constant, and  $T$  is the temperature. Viscosity at the reference temperature  $T_0$  and stress  $\sigma_0$  is denoted as  $\eta_0$ , and we set  $T_0$  as the temperature at the boundary between the two layers. Near the boundary ( $z = 0$ ), viscosity can be approximated by

$$\eta \approx \eta_0 \exp \left( -\frac{\alpha E}{nRT_0^2} z \right) = \eta_0 \exp \left( -\frac{z}{L} \right), \quad (4)$$

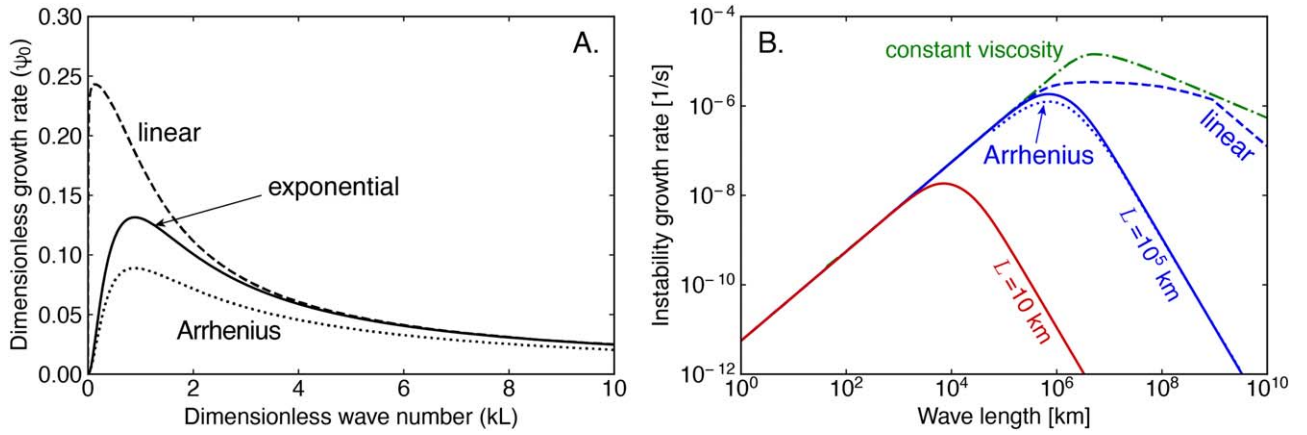


**Figure 1.** Dispersion relations of the RT instability for a denser viscous layer overlying a lighter one. (A) Nondimensionalized growth rate ( $\psi_0$  in Equation (7)) as a function of dimensionless wavelength ( $kL$ ). Three different viscosity profiles are considered: exponential,  $\eta = \eta_0 \exp(-z/L)$ , solid; linear,  $\eta = \eta_0(1 - z/L)$ , dashed; and Arrhenius,  $\eta = \eta_0 \exp(E/R(1/T - 1/T_0))$ , dotted. All three cases have the same viscosity derivative at the interface ( $\eta/(d\eta/dz) = -L$ ). For the Arrhenius profile, a linear temperature increase is postulated, leading to a steeper viscosity increase than an exponential profile. (B) The same as (A) but plotting results of exponential viscosity profiles with dimensions for  $\eta_0 = 10^{16}$  Pa s,  $\Delta\rho = 1000$  kg m $^{-3}$ , and  $g = 1.4$  m s $^{-2}$ . Colors indicate different viscosity scale height thicknesses (10 km, red;  $10^5$  km, blue), and a case for constant viscosity is also shown (green; Chandrasekhar 1961). Results for different viscosity profiles are also plotted for the case of  $L = 10^5$  km, showing that exponential and Arrhenius profiles exhibit nearly identical growth rates under the same viscosity derivative.

where  $\alpha$  is the first-order temperature derivative ( $T \simeq T_0 + \alpha z$ ) and  $L$  is the scale height of viscosity ( $nRT_0^2/(\alpha E)$ ). The dispersion relation for such a system can be obtained by solving the following differential equation:

$$\left[ \left( \frac{d^4}{dz^4} - 2k^2 \frac{d^2}{dz^2} + k^4 \right) + 2 \frac{d\eta}{dz} \frac{d}{dz} \left( \frac{d^2}{dz^2} - k^2 \right) + \frac{d^2\eta}{dz^2} \left( \frac{d^2}{dz^2} + k^2 \right) - \frac{\psi\rho}{\eta} \left( \frac{d^2}{dz^2} - k^2 \right) \right] u_z = \frac{u_z g k^2 d\rho}{\psi\eta dz}, \quad (5)$$

where  $k$  denotes the wavenumber of the small-amplitude perturbation,  $\rho$  is the density,  $\psi$  is the growth rate of the instability, and  $u_z$  is the vertical velocity. For ice and silicates, viscosity is sufficiently high that the  $\psi\rho/\eta$  term is usually negligible, and the dispersion relation for such cases has been derived by Conrad & Molnar (1997). Ignoring the  $\psi\rho/\eta$  term in Equation (5), originating from the acceleration term, only underestimates the maximum growth rate by a negligible factor because  $\psi \ll (\eta/\rho)k^2$  for any viscosity of interest. We note that the same equation has been used to solve for crater relaxation with  $d\rho/dz = 0$  (Parmentier & Head 1981).

The solution for Equation (5) depends on boundary conditions, in particular on the relative values of the two important length scales in the problem,  $L$  and the crustal thickness,  $h$ . In most instances,  $L$  is very small, so it is of interest to consider the case where  $L \ll h$ . In this case, the surface does not matter and the problem becomes nearly identical to that of the two-layer system, with both layers infinite in vertical extent. This is because the eigensolutions in the upper layer decay to negligible values at the free surface, and the thickness of the upper layer  $h$  has virtually no influence on the instability timescale. For this, the two-layer system is most unstable under a perturbation of a wavelength (Figure 1;

Conrad & Molnar 1997)

$$\lambda = \frac{2\pi L}{\Lambda_0} = \frac{2\pi nRT_0^2}{\Lambda_0 \alpha E}, \quad (6)$$

where  $\Lambda_0$  is a factor on the order of 1, and its growth rate  $\psi$  is approximately given by

$$\psi = \psi_0 \frac{\Delta\rho g L}{\eta_0}, \quad (7)$$

where  $\Delta\rho$  is the density difference between the two layers, and  $\eta_0$  is the viscosity at the boundary. The factor  $\psi_0$  is on the order of 0.1, and  $\psi_0$  is insensitive to the viscosity derivative of orders higher than 2. Even under a linear change in viscosity ( $\eta = \eta_0(1 - z/L)$ ),  $\psi_0$  increases only to  $\sim 0.3$ , and adopting a steeper viscosity profile shows a minimal decrease of  $\psi_0$  (Figure 1). For example, the actual viscosity profile of a crust is determined by temperature through an Arrhenius formulation, which yields a steeper viscosity increase compared to an exponential profile. The dispersion relation for such a case can be calculated using a propagator matrix method (Hager & O'Connell 1981; Mondal & Korenaga 2018), but the results reveal that  $\psi_0$  decreases only by a factor of  $< 2$  (Figure 1). Employing Equation (7) therefore suffices for estimating the instability timescale, and the local viscosity change close to the boundary mostly determines the stability of the upper layer.

In the other limit,  $L \gg h$ , the upper layer behaves as if it were of constant viscosity, and the preferred scale of the instability is of order  $h$ . When a layer with a thickness  $h$  is overlying a lighter infinitely thick one, the growth rate of the instability is

$$\psi = \psi_0 \frac{\Delta\rho g h}{\eta_0}, \quad (8)$$

and the most unstable mode has a wavelength of  $\lambda \simeq 2\pi h$ . The similarity between Equations (7) and (8) arises because, for a depth-dependent viscosity, the flow will be confined within the viscosity scale height, and not the entire crust, due to the

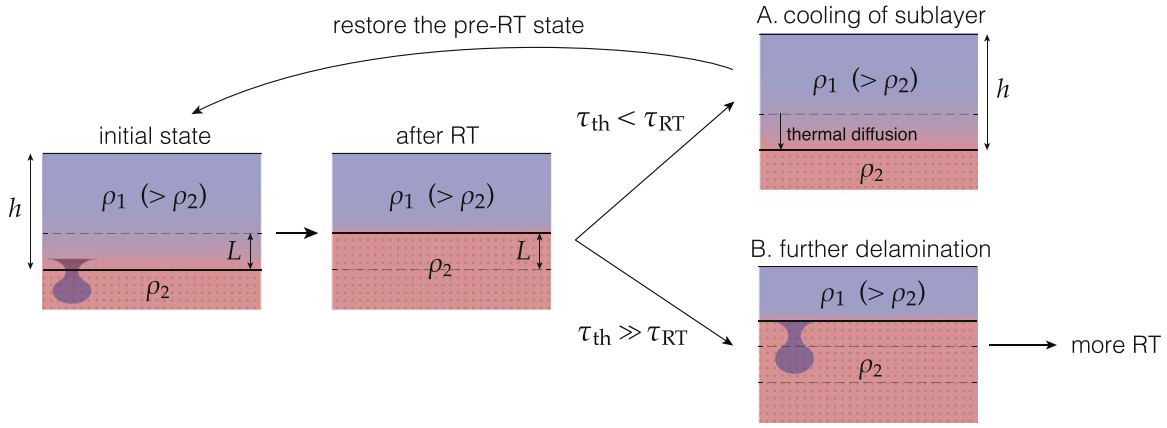


**Figure 2.** Schematic illustration describing the aftermath of the RT instability, distinguished by the respective magnitudes of diffusion ( $\tau_{th}$ ) and instability timescales ( $\tau_{RT}$ ). (A) For  $\tau_{th} < \tau_{RT}$ , thermal diffusion swiftly reestablishes the initial thermal structure prior to the onset of the instability. If a phase transition accounts for the crust–mantle density difference, as seen in Io’s magma ocean, thermal diffusion will reinstate the thickness of the dense crust, leading to the repeating instabilities at the same depth. These instabilities will be contained in the thin layer at the bottom and do not destabilize the entire crust. (B) For  $\tau_{th} \gg \tau_{RT}$ , the instability can propagate to the shallower regions, potentially destabilizing the entire crust. Temperature is illustrated using colors (blue, cold; red, hot), and regions occupied by lighter materials are represented with dots.

rapidly changing viscosity. This could be important since thermal relaxation could readily cool the replaced layer as quickly as it peels away, provided  $\psi L^2/\kappa \lesssim 1$ , where  $\kappa$  is the thermal diffusivity (Section 2.2).

The preceding calculations assumed no viscosity difference across the boundary between the two layers, but the viscosity of the lower layer has a negligible effect on the instability timescale (Figure 1; Conrad & Molnar 1997). A less viscous lower layer merely reduces the instability timescale by a factor of  $\sim 1$ . While a non-Newtonian viscosity may produce a faster super-exponential growth of the perturbation, its impact on the timescale is also small. Numerical experiments by Molnar et al. (1998) have demonstrated that the overall growth rate can be described as (Rubin et al. 2014)

$$\psi = \frac{0.76(n-1)^{1/n}}{2n} \left( \frac{Z_0}{L} \right)^{1-1/n} \frac{\Delta\rho g L}{\eta_0} \quad (9)$$

for  $L \ll h$ , where  $Z_0$  is the initial amplitude of the perturbation at the crust–mantle boundary. While the timescale depends on the initial state in a non-Newtonian system, typical values of  $n=2$  and  $Z_0/L=0.1$  yield a pre-factor  $\psi_0$  of  $\sim 0.06$ , which does not significantly differ from the results in Figure 1. Unless the initial amplitude is minimal,  $Z_0$  only has a modest effect on the growth rate  $\psi$  for  $n < 2$ .

## 2.2. Aftermath of the Rayleigh–Taylor Instability

For the case of  $L \ll h$ , the RT instability involves only a region of thickness  $\sim L$ , and the onset of the instability does not necessarily result in the foundering of the entire crust. Instead, the RT instability peels off a layer with a thickness  $L$  from the crustal base, creating a new sublayer through upwelling, while thermal diffusion eases the temperature jump created at the detached boundary (Figure 2). Depending on the diffusion timescale, the aftermath of the instability can vary considerably.

The two relevant timescales are the diffusion timescale,  $\tau_{th} = L^2/\kappa$ , and the time needed to trigger another RT instability,  $\tau_{RT} (=1/\psi)$ , which can be estimated from the growth rate of the instability. When  $\tau_{th} < \tau_{RT}$ , thermal diffusion quickly reverts the thermal structure to the state prior

to the onset of the instability. If a compositional difference accounts for  $\Delta\rho$ , a newly formed sublayer would be neutrally buoyant, shifting the possible instability to shallower depths where the timescale is even longer (cases of dirty ice on icy satellites). In contrast, if a phase transition is responsible for  $\Delta\rho$ , as is the case with Io’s magma ocean (Section 4), thermal diffusion and crustal subsidence also restores the density structure preceding the onset of the instability. Another instability will be triggered after  $\tau_{RT}$ , but each time the initial state is promptly restored by thermal diffusion, despite the successive delamination of the crustal base (Figure 2(A)). In either scenario, the RT instability is confined to the bottom layer with a thickness  $L$  and does not result in the destabilization of the entire crust.

On the other hand, under  $\tau_{th} \gg \tau_{RT}$ , another RT instability may be triggered before restoring the initial thermal profile, leading to the further removal of the shallower region of the crust (Figure 2(B)). The condition  $\tau_{th} > \tau_{RT}$  can be expressed as

$$L > \left( \frac{\eta_0 \kappa}{\Delta\rho g} \right)^{1/3} \equiv L_{crit}, \quad (10)$$

where a critical length  $L_{crit}$  is in the range of 1–10 km for the problems discussed in this study ( $\eta_0 = 10^{17-20}$  Pa s,  $\Delta\rho \sim 100$  kg m $^{-3}$ , and  $g \sim 1$  m s $^{-2}$ ). For an icy crust, the viscosity scale height  $L$  also falls on the order of 1–10 km, whereas  $L$  is less than 100 m for Io, rendering the condition of  $L \gg L_{crit}$  and  $\tau_{th} \gg \tau_{RT}$  unlikely to be satisfied for many scenarios (Section 3.4). This suggests that, for the cases of  $L \ll h$  in small-body settings, the RT instability is most likely to be confined to the lowermost part of the crust and thus would not be visible at the surface.

## 3. Application to Icy Satellites

We apply the equations above to examine the stability of the rock-contaminated icy crustal layer, which likely exists at the surface of Ganymede and Callisto. Equation (7) highlights the dependence of the instability timescale on the viscosity at the crust–mantle boundary  $\eta_0$  and the scale height of viscosity  $L$ .



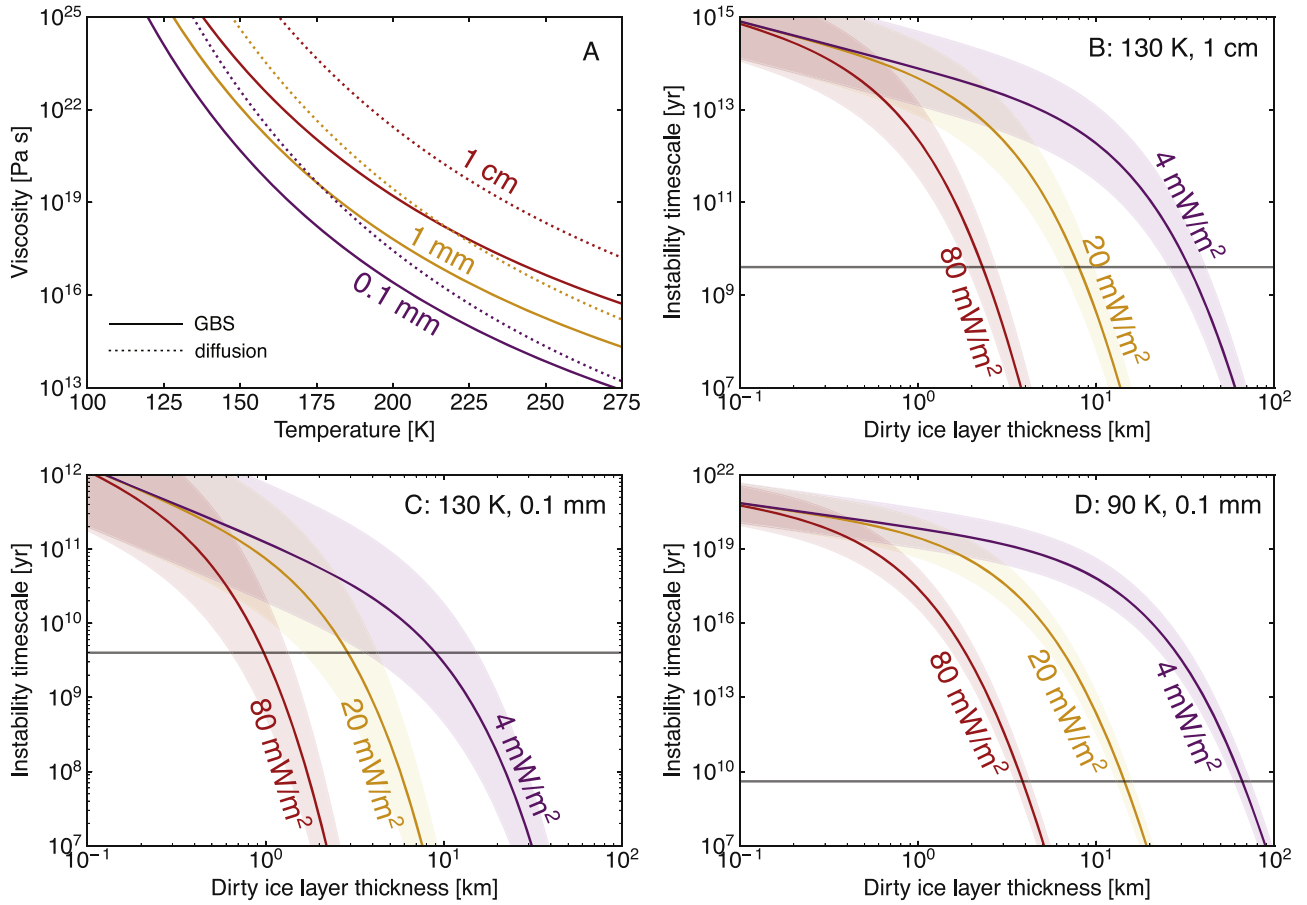


**Figure 3.** (A) The effective viscosity of ice I adopted from Goldsby & Kohlstedt (2001) and Bland et al. (2009) as a function of temperature  $T$  for diffusion creep (dotted) and grain boundary sliding (GBS; solid) under a shear stress of 0.1 MPa. Three different grain sizes (0.01 mm, purple; 1 mm, orange; 10 cm, red) are considered here. (B)–(D) The instability timescale of a dirty-ice layer as a function of thickness  $h$  for  $g = 1.4 \text{ m s}^{-2}$  and  $\Delta\rho = 100 \text{ kg m}^{-3}$ . Timescale is calculated for three surface heat flux values: 80 (red), 20 (orange), and  $4 \text{ mW m}^{-2}$  (purple). Viscosity is estimated based on two different grain sizes ((B) 1 cm; (C)–(D) 0.1 mm) and a shear stress of 0.5 MPa, and shaded areas delineate when the shear stress varies between 0.05 and 5 MPa. The surface temperature assumed in (D) ( $T_s = 90 \text{ K}$ ) is lower than in (B) and (C) ( $T_s = 130 \text{ K}$ ). The age of the solar system (4.5 Gyr) is shown as a reference (gray). Whereas the decreasing trend in timescale for small  $h$  values can be attributed to the explicit effect of the thickening crust  $h$ , its rapid decrease for larger  $h$  values is due to the temperature-induced reduction in  $\eta_0$ .

Whereas the value of  $L$  for Ganymede and Callisto falls between 0.1 and 10 km,  $\eta_0$  can change by many orders of magnitude depending on temperature (Figure 3(A)). Because of its implicit relevance to  $\eta_0$ ,  $T_s$  and  $h$  are crucial for this problem: If the surface is cold and/or the dense near-surface layer is thin, the viscosity at its base is large (far larger than the value one would associate with convection to carry the heat at much greater depths). The heat flux is also important but becomes less significant with a smaller  $h$  because the temperature at  $h < 1 \text{ km}$  is not hugely different from  $T_s$  for any reasonable heat flux.

The dirty-ice layer becomes increasingly unstable as its thickness increases. If the dirty ice extends to a 10 km depth, the crustal base has to be sufficiently viscous to be consistent with the age of a dark terrain and a high surface heat flux in the past, which requires a reasonably large grain size ( $> 1 \text{ cm}$ ; Figure 3(B)). The influence of the RT instability, however, is likely to be contained within the crustal base for most cases and does not destabilize the entire crust because the instability only erodes the lowermost part of the crust. The newly formed layer that replaces the delaminated portion can quickly cool by thermal diffusion, and another instability may take much longer to operate (Figure 4). In the following, calculations on the

instability timescale are outlined after summarizing our assumptions on rheology and thermal structure.

### 3.1. Rheology of the Icy Crust

Viscosity is a strong function of temperature and is known to take the following Arrhenius form:

$$\eta = \frac{\sigma}{\dot{\epsilon}} = \frac{A p^p}{\sigma^{n-1}} \exp\left(\frac{E}{RT}\right), \quad (11)$$

where  $\sigma$  is shear stress,  $A$  is the pre-exponential factor, and  $p$  is the grain size exponent. Goldsby & Kohlstedt (2001) constrained the parameters for different creep mechanisms of ice I, and the values of  $A$ ,  $p$ ,  $n$ , and  $E$  are adopted from the compilation by Bland et al. (2009). In the crust of Galilean satellites, characterized by temperatures below 180 K and a typical stress of 0.1–1 MPa, grain boundary sliding is the weakest deformation mechanism, and diffusion creep could be significant near the melting temperature (Figure 3(A); McKinnon 2006), although the extrapolation of the experimental data may be imprecise or incorrect. These two creep mechanisms are considered, and for these mechanisms grain

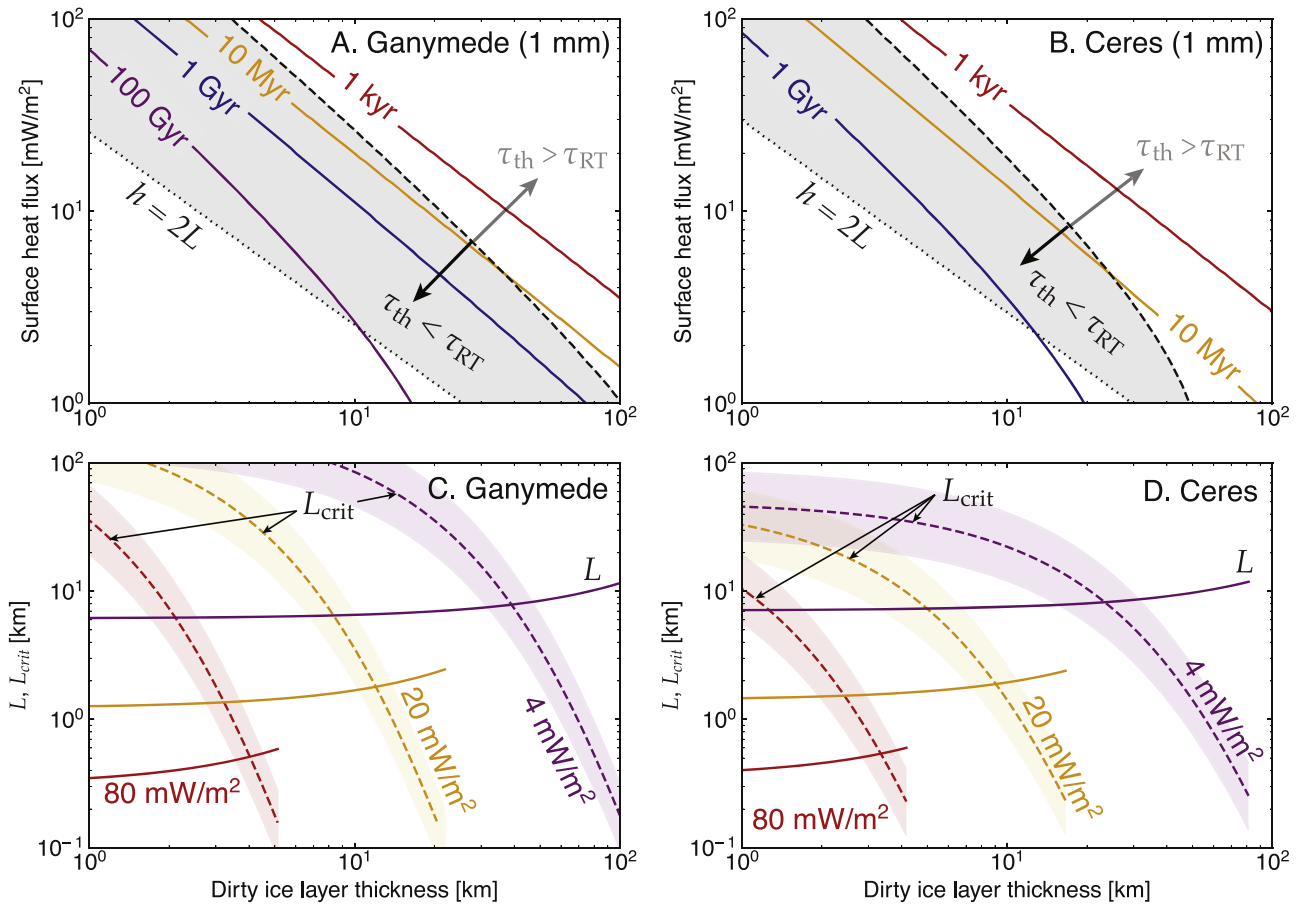


**Figure 4.** (A), (B) Contours of the instability timescale as a function of dirty-ice layer thickness and the surface heat flux for two different surface temperatures: (A) 130 K, relevant to Ganymede and Callisto ( $g = 1.4 \text{ m s}^{-2}$ ), and (B) 150 K, relevant to Ceres ( $g = 0.27 \text{ m s}^{-2}$ ). A grain size of 1 mm, a background stress level of 0.5 MPa, and  $\Delta\rho = 100 \text{ kg m}^{-3}$  are assumed. A dashed line separates the two different regimes after the onset of the RT instability ( $\tau_{th} \lesseqgtr \tau_{RT}$ ). In the upper-right region ( $\tau_{th} \gg \tau_{RT}$ ), repeating instabilities are possible, resulting in the destabilization of the entire crust, whereas in the gray region ( $\tau_{th} < \tau_{RT}$ ), the newly formed sublayer rapidly cools, and the instability only delaminates a layer of thickness  $L$ . Toward the lower-left corner, the viscosity scale height and the crustal thickness become comparable (dotted lines of  $h = 2L$  are shown as a reference), and the instability should result in some resurfacing. (C), (D) The viscosity scale height  $L$  and the critical length  $L_{crit}$ , defined in Equation (10), are plotted for three different surface heat fluxes: 80 (red), 20 (orange), and  $4 \text{ mW m}^{-2}$  (purple). Shaded areas delineate when the shear stress varies between 0.05 and 5 MPa, with the middle line representing 0.5 MPa, and a grain size of 1 mm is assumed.

size and stress level become undoubtedly important, given their potential to change viscosity by orders of magnitude.

Given the uncertainties within icy satellites, we test a range of values for grain size and background stress; grain size is expected to fall in the range of 0.1 mm–1 cm if grain growth is suppressed by impurity (Barr & McKinnon 2007). Grain boundaries can be pinned by even smaller rocky grains for a rock-ice mixture, so a small grain size is indeed expected. Stress in an ice shell is usually characterized by tides (0.1–a few MPa; Nimmo & Gaidos 2002), but the stress relevant to small-scale RT instability can be different from long-wavelength tidal stress. If the stress is localized at large-scale block edges, the background stress pertinent to the instability would be somewhat lower than tidal stress. From these considerations, stress levels ranging from 50 kPa to 5 MPa are adopted in the following calculations. The expected interplay between grain size and stress may complicate the issue, but the overlap between the observations in terrestrial ice sheets, also influenced by impurities (De La Chapelle et al. 1998), provides some confidence in the estimations. The calculations presented here are based on pure ice I rheology (Goldsby & Kohlstedt 2001) because the viscosity of the ice-rock mixture should resemble that of pure ice as long as the rock does not

occupy a critical volume (Durham et al. 2010). The same could be said for the presence of salts, although the concentration of ammonia may introduce some complexity (Durham et al. 2010). The critical volume may vary by an order of magnitude, depending on the deformation mechanism, material strength, and geometric arrangements. For grain boundary sliding, it has been suggested that even a small amount of impurity ( $\sim 6\%$ ) could significantly restrict deformation (Qi et al. 2018), which could potentially enhance the stability of the dense crust (see Section 7.1).

### 3.2. Thermal Profile of the Icy Crust

The crustal base temperature is estimated by assuming a range of surface temperatures and heat fluxes. Heat transport within the near-surface layer is primarily conductive, and thus the thermal gradient can be calculated from the surface heat flux. As the thermal conductivity of ice takes the form  $k_T = D/T$  ( $D = 632 \text{ W m}^{-1}$ ; Andersson & Inaba 2005) for clean crystalline material, the temperature within the conductive layer is described as  $T(z) = T_s e^{qz/D}$ , where  $T_s$  is the surface temperature,  $q$  is the surface heat flux, and  $z$  is the distance from the surface. A higher temperature gradient might arise if the ice is dirty or somewhat amorphous (Andersson &

Inaba 2005), although this may only matter at the lowest end of the temperature range of interest. We assume a range of surface temperatures (90–170 K) in the following, which covers the temperature of interest from the coldest region of Ganymede to the hottest of Ceres.

For our purposes, the “surface” temperature means the temperature below the diurnal variation in the thermal skin depth, typically less than a few meters, with actual surface temperatures varying with time of day. Surface temperature below the diurnal layer is also heterogeneous and varies by local albedo and latitude (Brown et al. 2023). On Ganymede, the dark terrain, with its lower albedo, records higher surface temperatures (120–130 K) than the brighter grooved terrain ( $\sim 100$  K) at the same latitude ( $0^\circ$ – $30^\circ$ ), and the polar regions exhibit much colder surface temperatures of  $< 90$  K. Such lateral variation in surface temperature persists throughout the depth of the conductive layer and impacts the instability timescale (Figure 3).

### 3.3. Stability of the Icy Crust

With knowledge of rheology and thermal structure, the instability timescale can be calculated for various thicknesses of the rock-contaminated (dirty ice) layer  $h$  (Figures 3(B)–(D)). For simplicity, we assume that the top  $h$  meter is heavier by  $\Delta\rho$  than the underlying pure ice layer. For small  $h$  values, the viscosity at the boundary ( $\eta_0$ ) remains mostly unchanged, and the explicit effect of  $h$  leads to a linear decrease in the instability timescale ( $\psi \sim h$  in Equation (8)). Meanwhile, the instability timescale decreases more rapidly due to the temperature effect for larger  $h$  values. The instability timescale is shaped by  $\eta_0$  rather than  $L$  (viscosity scale height; Equation (7)) as the latter remains mostly constant throughout the crust. With a thicker dirty-ice layer  $h$  and a higher surface heat flux  $q$ , the boundary temperature increases, causing a decrease in the instability timescale.

For crusts thinner than 1 km, the base temperature does not significantly differ from the surface, so a dense crust remains stable for a long term ( $> 4$  Gyr) under a wide range of plausible combinations of surface heat flux, background stress levels, and grain sizes (Figures 3(B), 4(A)). In contrast, as heavy crusts become thicker than 1 km, the value of surface heat flux starts to influence the instability timescale. The present-day heat flux of Ganymede is likely to be bounded by the radiogenic heat production in a rock core, and this estimate is consistent with a depth of ice I–ocean transition of  $\sim 100$  km, yielding a heat flux of  $\sim 4$  mW m $^{-2}$  (a temperature gradient of  $\sim 1$  K km $^{-1}$ ; Vance et al. 2014). Callisto and Ganymede are expected to have similar present-day fluxes, considering their rock fractions and only a slight difference in sizes. Such a low flux can sustain a 10 km thick dense crust for the age of the solar system even under low grain sizes ( $\sim 0.1$  mm) and in the dark regions of icy bodies ( $T_s = 130$  K; Figure 3(C)).

The topography of Ganymede, however, suggests that heat flux during the active tectonic period could have been as high as  $\sim 100$  mW m $^{-2}$  with a lithosphere of  $\sim 1$  km (Nimmo et al. 2002). Such a high flux during the early history implies that a dirty layer thicker than  $> 10$  km would be unstable and experience an overturn unless the grain size is very large ( $> 10$  cm). Regarding the value of  $h$  on Ganymede, craters on the dark terrain with a diameter smaller than 50 km, having floors with similar albedo to the surface on which they formed, indicates that rock contamination extends to a depth of  $\sim 10$  km

(Parmentier et al. 1982). If so, for the dark terrain to be stable for a billion-year timescale, the grain size of Ganymede’s crust has to be sufficiently large and/or the stress level to be low to prevent an overturn, and a small change in grain size or stress levels could disturb the crustal stability. With some observations on the dirty-ice layer thickness, some constraints may be placed on the rheology of the icy crust in the dark terrain. The crater size distribution on Callisto also implies a higher surface heat flux ( $\sim 40$ – $50$  mW m $^{-2}$ ) during the earlier period (Bjornnes et al. 2022). A thick dirty-ice layer ( $\sim 100$  km) may emerge as a consequence of incomplete differentiation (Nagel et al. 2004), but such a crust is prone to gravitational instability and is unlikely to survive until the present day (Figure 3(B)).

The surface features on Callisto and Ganymede’s dark terrain date back to  $> 4$  Gyr (Greeley et al. 2000; Zahnle et al. 2003), suggesting that the dirty-ice layer has survived for billions of years, including the period of a high surface heat flux (Nimmo et al. 2002; Bjornnes et al. 2022). While a dirty-ice layer of several kilometers in thickness can remain stable over the age of the solar system under a wide range of conditions, a layer of  $> 10$  km thickness would require a specific set of conditions (large grain size, low stress level) to ensure its survival. Further constraints on the dirty-ice layer will enhance our understanding of the properties of the icy crust on Ganymede and Callisto.

While the discussions above assumed a surface temperature of 130 K, a colder surface exhibits a stronger potential to stabilize a dense crust. Whereas the value of  $T_s = 130$  K is relevant to Ganymede’s dark terrain and mostly dark Callisto, the surface temperature drops below 90 K in the poles and in the grooved terrain of Ganymede due to its higher reflectivity (Brown et al. 2023). The instability timescale in colder regions becomes longer than in warmer ones by a factor of  $\sim 10$  under the same grain size and stress levels. Consequently, a  $\sim 10$  km thick rock-contaminated layer can survive under a wider range of conditions (Figure 3(D)). On the other hand, for a surface temperature of  $> 150$  K relevant to Ceres, a 10 km thick dense crust can be destabilized within 100 Myr for small grain sizes ( $< 1$  mm) with a temperature gradient of 2 K km $^{-1}$  (Hesse & Castillo-Rogez 2019; Figure 4(B)). Rock contamination is thus likely to be contained within a thin layer near the surface, and this layer is expected to have small grain sizes and/or low stress levels, especially in the warmer region of Ceres. In the even warmer interior, the RT instability operates on a short timescale, and the exposures of Na carbonate on Ceres may be attributed to the upwelling due to the instability (Stein et al. 2023).

### 3.4. Crustal Resurfacing by the RT Instability

The onset of the RT instability does not necessarily result in overturning the entire crust unless the temperature of the crustal base is sufficiently high (Section 2.2). For high viscosities ( $\eta_0 > 10^{20}$  Pa s), the critical length  $L_{\text{crit}}$ , defined by Equation (10), is greater than 10 km, exceeding the viscosity scale height  $L$  (Figure 4(C)). In such cases, thermal diffusion cools the newly formed sublayer that replaces the delaminated part of the crust before the growth of another RT instability ( $\tau_{\text{th}} < \tau_{\text{RT}}$ ). This keeps the new crust–mantle boundary at a shallower depth cold, and the development of another instability takes longer than the first one. Even if the instability operated on icy satellites in the past, its onset may have not resulted in any surface expressions.

If, on the other hand, the temperature at the crustal base is close to the melting temperature, viscosity becomes sufficiently low so that  $L_{\text{crit}} \gg L$  is satisfied ( $\tau_{\text{th}} \gg \tau_{\text{RT}}$ ). The instability may then be triggered repeatedly as the upwelling of warm materials heats the crust and leads to destabilizing the shallower part of the crust (Figure 2(B)). This scenario requires that the temperature at the crustal base is sufficiently high (Figure 4(A)), and a smaller grain size or higher stress level can further increase the likelihood of  $\tau_{\text{th}} \gg \tau_{\text{RT}}$ . Although many possibilities have been proposed for the formation of the grooved terrain, including a heat pulse (Kirk & Stevenson 1987) and the onset of stagnant-lid convection (McKinnon 2006), a scenario may also be possible wherein the grooved terrain resulted from a regional onset of the gravitational instability in areas with high heat flux, small grain size, and/or high stress levels, which triggered crustal foundering and resurfacing.

### 3.5. Additional Remarks

Although the instability timescale is by far most sensitively dependent on surface temperature  $T_s$  and heat flux  $q$ , it also inversely depends on the density difference between the topmost dirty ice and the underlying clean ice ( $\Delta\rho$ ). This difference could easily be small, perhaps a mere fraction of a percent, especially if the main cause is impacts. An impact event excavates a volume of ice that is far larger than the volume of the impactor, so the dirty impactor (plausibly 50% mixtures of ice and rock) is then strongly diluted by turbulent mixing with the excavated ice debris, most of which falls to the near surface around the crater (e.g., Croft 1980). The consequence is a smaller value of  $\Delta\rho$ , associated with a larger value for  $h$ . The latter has a large influence on the instability timescale despite  $\Delta\rho$  and  $h$  having competing effects. Whereas a smaller  $\Delta\rho$  only increases the instability timescale by some factor, a larger  $h$  can reduce the base viscosity  $\eta_0$ , and thus the instability timescale drops by orders of magnitude.

These timescales are calculated assuming a constant density for the upper layer with  $\Delta\rho = 100 \text{ kg m}^{-3}$ , but a more realistic density structure would not change the overall conclusion here. Considering a linear density decrease within the upper layer would only reduce the instability timescale by a factor of  $\sim 3$  (Conrad & Molnar 1997), and adopting a more realistic viscosity (steeper than exponential profile) does not influence the timescale as well (Figure 1(A)). We also note that the viscosity scale height is estimated to be shorter than  $\sim 5 \text{ km}$ , so the most unstable mode would have a wavelength shorter than  $50 \text{ km}$ . This is short enough on a planetary scale that the spherical effect is irrelevant to the crustal instability timescale.

## 4. Application to Io

If a subsurface magma ocean exists inside Io (Khurana et al. 2011; Miyazaki & Stevenson 2022) and the overlying layer is of similar composition, then a crust should be heavier than the underlying magma ocean layer. Can such a structure can be sustained for a geological time? Even if the layer underlying the crust is only a partial melt, the crust can be more dense than the underlying material with quite a high degree of melting ( $\phi \gtrsim 0.3$ ; Appendix A). Here, we show that a potentially heavy crust on Io could also survive for the age of the solar system.

### 4.1. Thermal Profile of Io's Crust

Other than the obvious difference in crustal composition between Io and other Galilean satellites, Io has a distinct crustal thermal structure. The presence of substantial topography despite very large observed heat flow strongly suggests that Io releases most of its heat through volcanic eruptions (heat pipes). If so, the crustal thermal structure is controlled by the balance between conduction and advection (O'Reilly & Davies 1981):

$$k_T \frac{d^2 T}{dz^2} - \frac{d}{dz}(\rho c_p v_z T) + Q = 0, \quad (12)$$

where  $c_p$  is the thermal conductivity ( $3.3 \text{ W m}^{-1} \text{ K}^{-1}$ ),  $v_z$  is the subsidence velocity of the crust due to continuous resurfacing, and  $Q$  is the volumetric internal heating rate. Assuming that the conductive heat flow at the surface is negligible, the temperature gradient can then be described as

$$\frac{dT}{dz} = A \exp\left(\frac{v_z z}{\kappa}\right), \quad (13)$$

where  $A$  is the constant of integration, determined by the boundary condition. The subsidence velocity  $v_z$  could be estimated from the surface heat flux (Veeder et al. 2012) and should be in the range of  $1.5 \pm 0.5 \text{ cm yr}^{-1}$  (Spencer et al. 2020). Equation (13) implies that the crustal temperature is constant for most of the depth, except at the base where it increases exponentially (Figure 5(A)).

The large temperature gradient at the crustal base creates a very small viscosity scale height, which would inhibit the growth of the RT instability. When the temperature at the base of the crust is  $T_b$ , the thermal gradient at the base is given by

$$\left. \frac{dT}{dz} \right|_{z=h} \cong \frac{T_b - T_s}{\kappa/v_z}, \quad (14)$$

and the viscosity scale height can be calculated as (Equation (4))

$$L = \frac{nRT_b^2}{E} \frac{\kappa/v_z}{T_b - T_s}, \quad (15)$$

which is independent of crustal thickness  $h$ .

While a small viscosity scale height hinders the growth of the instability, the rapid temperature increase at the crustal base will lead to a shorter RT timescale. Although the exact temperature of the base of the crust is uncertain, it must be close to the melting point of mantle material. The degree of melting increases with depth, and density approaches that of the mantle, making it challenging to strictly define the crust–mantle boundary. We instead assume a range of the base temperature  $T_b$  in the following, but regardless of how the crustal base is defined, the short viscosity scale height remains a crucial factor in understanding the RT instability of Io's crust (Section 4.3).

In reality, the crust and mantle must be separated by a thin transitional layer where melt transport shifts from convective to eruptive, where Equation (13) is inapplicable. Such a layer, however, is likely to be very thin ( $< a \text{ few } 100 \text{ m}$ ), and it has



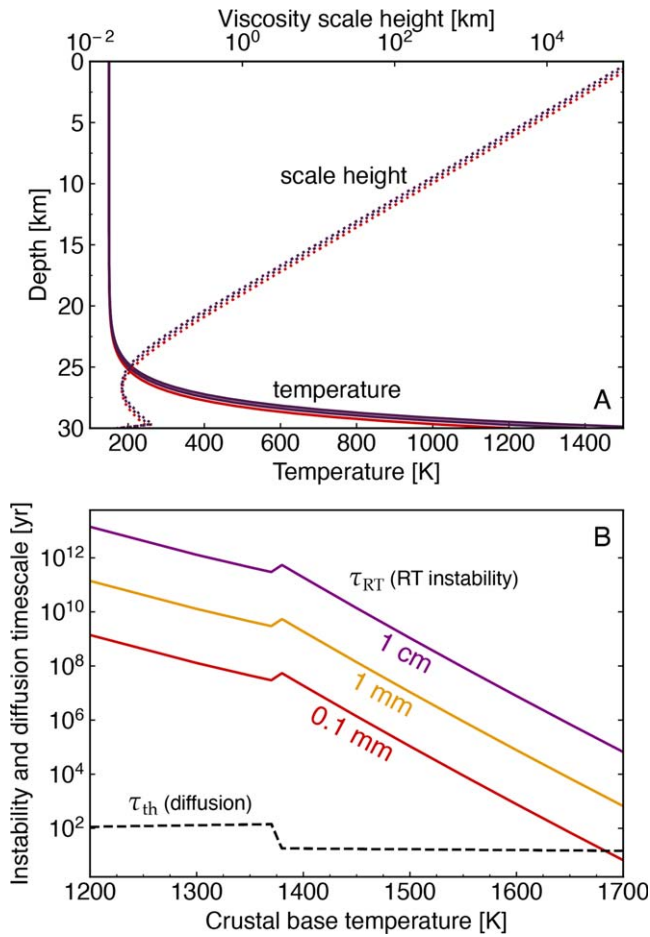


**Figure 5.** (A) The temperature profile within the crust of Io (solid) and the viscosity scale height ( $L$ , dashed), assuming a crustal thickness ( $h$ ) of 30 km and a crustal subsidence velocity of  $v_z = 2 \text{ cm yr}^{-1}$ . Colors indicate different temperatures assumed at the base of the crust, but their differences are insignificant. (B) The growth timescale of the RT instability ( $1/\psi$ ) as a function of the base temperature of the crust. Three different grain sizes are assumed: 0.1 mm (red), 1 mm (orange), and 1 cm (purple). The instability timescale ( $\tau_{RT}$ ) increases with the square of the grain size but does not depend on the crustal thickness  $h$ . The diffusion timescale ( $\tau_{th}$ ) needed to restore the thermal structure after the onset of the instability is also shown (black dashed), which is shorter than  $\tau_{RT}$  for a wide range of parameters.

little effect on the instability timescale estimate. A small layer thickness can be predicted from the fact that cold subsiding crust is heated by the latent heat of upwelling melt (Miyazaki & Stevenson 2022).

#### 4.2. Rheology of Io's Crust

The dominant creep mechanism for deforming silicate components changes from dislocation to diffusion creep at high temperatures ( $T > 900\text{--}1300 \text{ K}$ ; Mei et al. 2010; Jain et al. 2019). If a subsurface magma ocean exists, the base of the crust would have a temperature close to its melting point, and thus adopting diffusion creep ( $n = 1$  and  $E = 300 \text{ kJ mol}^{-1}$ ) becomes appropriate to discuss the crustal stability for this context (Mei & Kohlstedt 2000; Jain et al. 2018). With the base of the crust being colder than the solidus of peridotite (e.g., Katz et al. 2003), the viscosity scale height  $L$  would be on the order of 10–100 m (Figure 5(A)). The instability timescale does not depend on the crustal thickness  $h$  (Equation (15)) because of the small  $L$ , and the instability timescale could be longer than  $\sim \text{Gyr}$  (Figure 5(B)).

As in the case of icy materials, the instability timescale depends on grain size. The viscosity of materials undergoing deformation via diffusion creep can be described as

$$\eta = \eta_0 \left( \frac{d}{d_0} \right)^2 \exp \left( \frac{E}{R} \left( \frac{1}{T} - \frac{1}{T_0} \right) \right), \quad (16)$$

where  $\eta_0$  represents the reference viscosity at a grain size of  $d_0$  and a temperature of  $T_0$ . Deformation experiments and the small-scale convection beneath oceanic lithosphere collectively suggest a value of  $\eta_0 = 10^{19} \text{ Pa s}$  at  $T_0 = 1600 \text{ K}$  (Davaille & Jaupart 1994; Hirth & Kohlstedt 1996; Dumoulin et al. 1999) under a typical grain size of 1 mm (Faul & Jackson 2005). Equation (16) shows that the timescale changes with the square of the grain size, and when the grain size exceeds 1 mm the instability timescale can exceed the age of the solar system (Figure 5(A)).

#### 4.3. Stability of Io's Crust

While the RT instability timescale can extend beyond the age of the solar system for large grain sizes ( $> 1 \text{ mm}$ ) and a relative lower base temperature ( $< 1500 \text{ K}$ ), it largely depends on grain size and the temperature at the crustal base. Considering that extensive silicate melting is expected at the base with  $T_b > 1700 \text{ K}$ , and that a small grain size is feasible for Io due to insufficient grain growth time, the instability timescale can fall below  $10^7 \text{ yr}$  (Figure 5(B)).

Nevertheless, the onset of the RT instability does not indicate the destabilization of Io's floating crust. The instability results in the delamination of a thin layer at the crustal base, where its thickness is characterized by the viscosity length scale of  $L \sim 10\text{--}100 \text{ m}$  (Figure 5(A)). The thermal diffusion timescale across such a delaminated layer is less than 400 yr (Figure 5(B)), indicating that diffusion can swiftly restore the thermal structure soon after the onset of the instability (Section 2.2, Figure 2(A)). As the crust–mantle boundary is characterized by a phase transition on Io, the initial crustal thickness is also reinstated by thermal diffusion, with crustal subsidence also contributing. Therefore, the following scenario is plausible for Io's crust–mantle boundary: The RT instability causes a dripping of the thin bottom layer of the crust for numerous times, but each time thermal diffusion restores the initial thermal structure and crustal thickness. Despite a frequent onset of the RT instability, Io's heavy crust can remain stable on top of a magma ocean for a substantial period of time.

We note that the discontinuous change in diffusion and instability timescales at  $T_b \sim 1400 \text{ K}$  is caused by the melting effect (Figure 5(B)). Partial melt is known to reduce viscosity by a large factor that is complicated and composition dependent, but the reduction has been suggested to be as much as  $\exp(-26\phi)$  (Mei et al. 2002), where  $\phi$  denotes the melt fraction. This melt-induced effect lowers viscosity at the crustal base, as well as shortening the viscosity scale height. The viscosity scale height for a partially molten medium can then be described as

$$\frac{1}{L} = \frac{\alpha E}{RT_0^2} + 26\alpha \frac{d\phi}{dT}, \quad (17)$$

where the latter term reduces  $L$  by a factor of 10 in the case of Io (Figure 5(B)). The diffusion timescale ( $\sim 10\text{--}100 \text{ yr}$ ) thus

becomes much shorter than the time needed to trigger a RT instability (Section 2.2) for most sets of parameters (Figure 5(B)).

#### 4.4. Elastic Crust–Mantle Boundary

Most of the Io’s crust has a temperature close to the surface ( $\sim 150$  K), which is cold enough for the Maxwell time to be longer than the age of the solar system. This also applies to the uppermost crustal layer of the icy satellites. Under such circumstances, presuming a viscous upper layer would be inapplicable, instead the incorporation of elasticity emerges as a more appropriate consideration. Elasticity serves as a counterbalancing force against the gravitational effects due to density inversion, and especially for short wavelengths, the gain in elastic energy due to perturbation becomes larger than the release in gravitational energy. The system is stable against perturbations for wavelengths smaller than (Terrones 2005)

$$\lambda < \frac{8\pi\mu_1}{\Delta\rho g} \equiv \lambda_c, \quad (18)$$

where  $\mu_1$  is the shear modulus of the upper layer. This derivation assumes that the elasticity of the lower layer is negligible, but the lower layer having a nonzero rigidity only has a trivial influence on the critical wavelength,  $\lambda_c$  (Figure 8).

Having a finite-thickness upper layer could further limit the onset of instability for elastic layers. When the upper layer is thinner than the critical wavelength ( $h < \lambda_c/2\pi$ ), the upper layer is stable against any wavelength. Even when thicker, the instability is only triggered for a wavelength longer than the critical wavelength (Appendix B, Figure 8(A)). When the criterion above is applied to Io, we find that its lithosphere is stable against perturbations of  $\lambda \lesssim 10^6$  km, assuming  $\mu_1 = 20$  GPa,  $\Delta\rho = 400$  kg m $^{-3}$ , and  $g = 1.5$  m s $^{-2}$ . This criterion may even be applied to the elastic portion of Ganymede, where the Maxwell time can be on the order of billion years. For typical values for icy satellites ( $\mu_1 = 1$  GPa,  $\Delta\rho = 100$  kg m $^{-3}$ , and  $g = 1.4$  m s $^{-2}$ ), a critical wavelength of  $\sim 10^5$  km is obtained. The shear modulus of an elastic ice layer may be reduced by fracture or porosity, and field observations suggest that the shear modulus of ice shells may be somewhat lower than that of intact ice ( $\sim 4$  GPa; Gammon et al. 1983; Nimmo 2004). Yet, these critical values are considerably larger than the radius of Io (1821 km) or Ganymede (2631 km), indicating that perturbations within Galilean satellites are too short to induce the RT instability. The value for Earth ( $10^4$  km) is also larger than the radius, and, in short, no instability is possible for a purely elastic shell on solar system objects.

##### 4.4.1. Analogy to Tidal Distortion

This problem is closely analogous to the well-studied problem of the tidal distortion of a fluid sphere overlain by a spherical elastic shell, which is a popular model for Io and Europa (e.g., Cassen et al. 1979; Peale et al. 1979). First, let us consider the simple case of a homogeneous elastic sphere of radius  $R$ . For a surface height modulation of order  $l$ , the gravitational energy is of order  $\rho g l^2 R^2$ . For the longest possible wavelength instabilities (degree 2 for tides), the elastic energy has an order of  $\mu(l/R)^2 R^3$  because the strain is of order  $l/R$ . These energies are comparable when  $\mu \approx \rho g R$ , where the dimensionless number  $\mu/\rho g R$  figures prominently in the classic work of Love (1909). This is much larger than unity for the

bodies of interest to us, indicating the large strain energy compared to the gravitational, whereas it is comparable to unity for Earth. If we were to consider instabilities of shorter wavelength  $\lambda$ , the strain is  $l/\lambda$ , and the elastic energy becomes even larger by an order of  $(R/\lambda)^2$  than the case of  $\lambda \approx R$ , despite strain being confined to a depth range comparable to  $\lambda$ . Qualitatively, this result would also apply to a density inversion (an “unstable” interface) inside a planetary body. Since elasticity is a stabilizing effect, this means that gravitationally driven instability does not happen within small, elastic bodies. Long-wavelength instabilities are less stable, but triggering instability would require a wavelength much larger than a planetary radius, which is impossible.

To obtain a qualitative understanding of the critical wavelength, let us consider an elastic shell with a thickness  $h$ , overlying an inviscid interior. As in the case of tides, a thin shell causes larger strains in the shell, which is why the Love number for Europa or Io can approach unity. Here, we assume a wave-like distortion of the interface in the interior (layer boundary) of order  $l$ , but we require that the distortion be negligible at the upper boundary to avoid the stabilizing effect of gravitational energy at the top surface (Equation (B6)). Under such circumstances, the strain is  $\sim l/h$ , and the total stored elastic energy is of order  $\mu(l/h)^2 R^2 h$ . Given that the gravitational energy release is  $\Delta\rho g l^2 R^2$ , instability can be triggered only under

$$h \gtrsim \frac{\mu}{\Delta\rho g}, \quad (19)$$

indicating that, for a sufficiently thin shell, strain energy is always large enough to avoid gravitational instability (Figure 8(A)) regardless of the wavelength. A linear stability analysis suggests a coefficient of  $8\pi$  in Equation (19).

It is tempting to imagine bending rather than internally deforming the shell, and such a flexural mode may indeed be relevant for some structures observed on icy satellites (Nimmo et al. 2002). This, however, does not contribute to the onset of instability because flexure implies a displacement of the upper (stabilizing) surface roughly the same as the displacement of the lower (destabilizing) surface with no net release in gravitational energy.

#### 5. Fracture Mechanisms and the Resulting Upwelling

A surface layer may be ruptured by stresses that are unrelated to the putative instability, where the most obvious candidates are impacts (O’Neill et al. 2017), tides (Greenberg et al. 2002), internal volume changes (Matsuyama et al. 2021), and convection (Gerya et al. 2015). Impacts can easily produce stresses of the same order of magnitude as  $\rho v_i^2$ , where  $v_i$  is the impact velocity, which easily exceeds the material strength. Although unlikely, the bodies of interest may have tidal stresses and convective stress larger than material strength, and this possibility has been hotly debated for Earth, especially where water can play a weakening role in rocks. Internal volume changes arising from thermal expansion or phase changes can easily create strains of a few percent but might be so slow that the response could be primarily viscous. In all cases, putative failure (cracking if the crust) is not sufficient to ensure foundering since any downward transport of that material, by continuity, has to be accommodated with some upwelling into the space created. There is no way of universally excluding this, but one useful way of considering this process

is to analyze the viscous flow through cracks or conduits created by foundering.

Let us assume that, at the beginning of the subsidence process, a crack conduit (with a width of  $\delta$ ) forms along a fault line, through which the mantle material will ascend with an upwelling velocity of (Turcotte & Schubert 2002)

$$w_{\text{up}} = -\frac{\delta^2}{12\eta} \frac{\partial p}{\partial z} \simeq \frac{\delta^2 \rho_0 g}{12\eta}. \quad (20)$$

Because the crustal temperature decreases toward the surface and cooling makes the material dramatically more viscous, the ascent has to be quick enough to avoid cooling by thermal diffusion:

$$\tau = \frac{h}{w_{\text{up}}} = \frac{12\eta}{\delta^2} \frac{h}{\rho_0 g} < \frac{\delta^2}{\kappa}. \quad (21)$$

When substituting a typical parameter relevant to icy satellites, we follow that

$$\delta > \left( \frac{12\eta\kappa h}{\rho_0 g} \right)^{1/4} = 1 \text{ km} \left( \frac{\eta}{10^{16} \text{ Pa s}} \right)^{1/4} \left( \frac{h}{10 \text{ km}} \right)^{1/4}, \quad (22)$$

where  $g = 1.4 \text{ m s}^{-2}$  is adopted. A kilometer-length width conduit has to be formed for the mantle ascent to take place, and thus even a partial subsidence of a dirty-ice layer is unlikely.

Because magma viscosity is orders of magnitude lower than the solid, the magma ascent on Io at first sight seems to occur much easier for melt rising from Io's magma ocean through its crust. For a mantle viscosity of 1 Pa s, the crack only needs to be less than 10 cm wide. When the crust is buried with newly erupted materials, the crust can partially subside by flexural bending, which could further open up the width of conduits for faster magma ascent (Figure 16 of Kemp & Stevenson 1996). Such a feedback mechanism has been suggested as a potential way to initiate subduction on Earth, but several factors could suppress such a phenomenon on Io: The large compressive stress within Io's crust (McKinnon et al. 2001; Kirchoff & McKinnon 2009) has been shown to limit the paths of magma ascent within the crust (McGovern et al. 2016). A mountain loading on the crust creates an ascent pathway of magma only in the vicinity of mountains, making the feedback between eruption and subsidence unlikely. Furthermore, the subsidence and crack widening due to mountain loading may be limited because the majority of Io's crust behaves elastically. These factors are likely to suppress the ascent of lighter materials through the crust, limiting the possibility of crustal foundering.

## 6. Impact Heating

Impact cratering can alter the thermal state of the mantle (Roberts et al. 2009; Watters et al. 2009) and has been proposed as a potential mechanism to initiate subduction on Earth (e.g., O'Neill et al. 2017). Impacts can create thermal anomalies, lithospheric thinning, and mantle upwelling; here, we investigate how thermal anomalies created by small impacts may influence the overturn between a dense crust and the underlying mantle. When the temperature increase penetrates throughout the crust, it may shorten the timescale for gravitational instability by lowering crustal viscosity.

Impacts into realistic planetary materials defy simple scaling laws, and numerical simulations are needed, but here we follow

the parameterization by Watters et al. (2009) to estimate the zeroth-order effect of impact heating. Consider that the crustal surface is hit by an impactor of a radius  $r_{\text{imp}}$  with a velocity of  $v_i$ . The impact creates a shock pressure of

$$P_s(r) = \frac{1}{4} \rho_0 (2C + S v_i) v_i \cdot \min \left( 1, \left( \frac{r_c}{r} \right)^{-1.84+2.61 \log v_i} \right), \quad (23)$$

where  $v_i$  is the impact velocity and  $r_c$  is the radius of an isobaric core ( $=0.451 r_{\text{imp}} v_i^{0.211}$ ). A temperature perturbation by impact,  $\Delta T$ , can be estimated from the following parameterization (Roberts et al. 2009; Watters et al. 2009):

$$C_p \Delta T = \frac{P_s}{2\rho_0 S} (1 - f^{-1}) - \left( \frac{C}{S} \right)^2 (f - \ln f - 1), \quad (24)$$

(the term  $\ln F$  in Watters et al. 2009 should be  $\ln f$ ), where

$$f(P_s) = -\frac{2SP_s}{\rho_0 C^2} \left( 1 - \sqrt{1 + \frac{4SP_s}{\rho_0 C^2}} \right)^{-1}. \quad (25)$$

Constants  $C$  ( $7.24 \text{ km s}^{-1}$ ) and  $S$  (1.25) are based on the mantle properties, assuming the Tillotson equation of state.

For impactors of a typical size colliding with Io and Ganymede ( $\sim 1 \text{ km}$ ) at velocities of  $20\text{--}30 \text{ km s}^{-1}$  (Zahnle et al. 2003), the resultant impact creates an isobaric core of  $r_c < 1 \text{ km}$ . In proximity to this isobaric core, the temperature disturbance exceeds 1000 K but rapidly diminishes away from the center, becoming negligible at  $r > 3r_c$ . In the absence of an atmosphere, such a molten region, which would be thinly distributed along the crater base, rapidly cools through blackbody radiation, and the temperature will drop below the melting point within at most  $\sim 100 \text{ yr}$ , even for very large impactors. While radiation and diffusion further cools the thermal anomaly, heating only penetrates by a limited extent. Therefore, for an impact to exert an influence on the instability timescale, the impactor has to be sufficiently large to propagate the temperature disturbance all the way to the crustal base, where a depth-dependent viscosity suppresses the growth of the instability. Whereas a relatively thin dense crust could easily be overturned (or excavated) by impacts, thicker crusts ( $> 10 \text{ km}$ ) are unlikely to be disturbed by a kilometer-size impactor. This scenario is likely to be the case for cratering dense crusts on icy satellites and Io, but larger-than-“typical” impactors are very much possible (albeit small in number). A body of radius 10 km has a 1000 times the mass and far bigger consequences, beyond the overturn of a dense crust.

## 7. Discussion and Conclusions

### 7.1. Moment of Inertia

Hydrostaticity does not enforce a principal moment of inertia less than  $0.4 MR^2$ , which is the value of a uniform-density sphere. It is sometimes thought that a top-heavy body cannot be hydrostatic, but the RT instability is simply a response to perturbations away from hydrostatic equilibrium and not a failure of hydrostaticity, which is the radial balance of weight with the pressure gradient force. While the principal moment of inertia can sometimes be obtained from geodesy (the determination of the rotational state of the body; e.g., Bills & Nimmo 2008), it is more usually estimated from the application of Radau–Darwin, which is only approximate and uses the



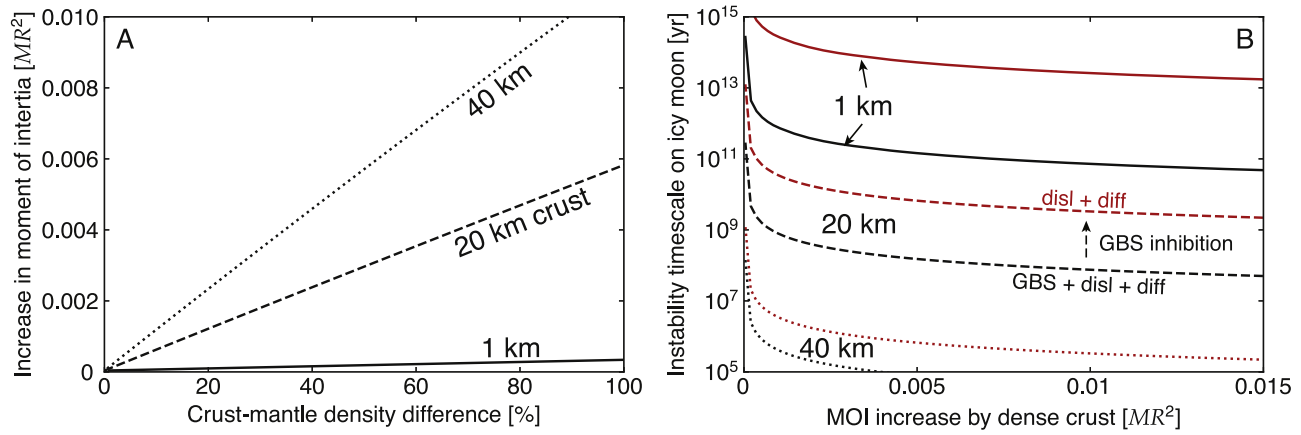


**Figure 6.** (A) The increase in moment of inertia by a dense crust plotted as a function of density difference between the crust and the underlying mantle. Three different crustal thicknesses (1 km, solid; 20 km, dashed; 40 km, dotted) are assumed. (B) The growth timescale of the RT instability (Equation (7)) as a function of the moment of inertia increase by a dense crust. Viscosity ( $\eta$ ) and its scale height ( $L$ ) are calculated based on a surface heat flux of  $8 \text{ mW m}^{-2}$ , a grain size of 0.1 mm, and a stress of 1 MPa. Because grain boundary sliding (GBS) is limited for  $\gtrsim 10\%$  contamination of silicate (Qi et al. 2018), the timescale is likely to follow the estimate based on diffusion and dislocation creeps (red). The instability timescale shown here is a lower bound estimate, and a dense crust of  $< 40 \text{ km}$  thickness could survive over geological time on icy bodies.

values of the degree 2 gravity harmonics, assuming hydrostaticity and a known perturbation including rotation and tides.

In our cases of interest (Io, Ganymede, and Ceres), the relevant data suggest a value substantially less than  $0.4 MR^2$  (Anderson et al. 1996a, 1996b; Park et al. 2016), primarily due to internal differentiation. This does not, however, indicate whether these bodies have a surface layer of greater density, which could be a potential source of increase to the moment. Within a reasonable range of density contrast, a dense crust of sufficient thickness ( $h > 10 \text{ km}$ ) could influence the moment of inertia by a small, but noticeable, degree. For instance, when a 40 km thick crust is contaminated with silicate by 25%, a density contrast ( $\Delta\rho/\rho$ ) of 50% can elevate the moment of inertia by  $> 0.005 MR^2$  (Figure 6(A)) and potentially more with a higher degree of rock contamination. Uncertainties in the moment of inertia are smaller than  $0.005 MR^2$  for Galilean satellites (Schubert et al. 2004), suggesting that the presence of such a dense crust could impact the interpretation of the moment of inertia observation, potentially leading to a smaller core radius. While it is improbable that contamination by impacts results in such a substantial crust–mantle density difference, incomplete differentiation could be the source for a substantial  $\Delta\rho$  (Nagel et al. 2004).

The viscosity at the base of a dense crust can be sufficiently high to delay the overturn of such a dense crust (Figures 3 and 4), maintaining an elevated moment of inertia for a geological timescale. Furthermore, an icy crust contaminated by  $\gtrsim 10\%$  silicate is more viscous than a purely icy one due to silicate grains impeding grain boundary sliding. Because grain boundary sliding is the weakest form of deformation in a typical icy crust (Qi et al. 2018), such an effect increases the instability timescale by 1–2 orders of magnitude (Figure 6(B)). Using Equation (7) to estimate the timescale, and assuming a grain size of  $0.1 \mu\text{m}$ , a stress of 1 MPa, and a surface heat flux of  $8 \text{ mW m}^{-2}$  (chosen to yield a lower bound estimate), a timescale of  $> 1 \text{ Gyr}$  is predicted for a 20 km thick dense crust on present-day Ganymede. For a larger grain size, smaller stress level, or smaller heat flux, a thicker crust would even survive for a billion-year timescale under the present-day thermal structure. With  $> 25\%$  contamination of silicates in a 40 km thick crust, the moment of inertia can increase by

$\sim 0.005 MR^2$ , indicating that a structure with an elevated moment of inertia could be ubiquitous among small icy bodies.

Even when the RT instability is triggered, it typically only peels off the lowermost part of the crust, allowing a dense crust to continue influencing the moment of inertia. For bodies like Io, which releases most of its energy through heat pipes, a dense crust with significant thickness can remain stable because the crustal temperature remains similar to the surface temperature for most of its depth (Figure 5(A)), and the instability timescale is independent of the crustal thickness. While a large density contrast is unlikely for silicate bodies, a thick dense layer with a large moment of inertia could in theory remain “stable” for billions of years.

## 7.2. Conclusion

A crust denser than the underlying mantle arises on planetary bodies through various mechanisms, including impact-induced rock contamination and incomplete differentiation. Despite the inherent gravitational instability of such structures, the growth timescale of the RT instability can extend to the age of the solar system due to the strong temperature dependency of viscosity. The small viscosity scale height resulting from such temperature dependency contributes to a prolonged growth timescale of the RT instability. It also limits the vertical extent of the instability, where the onset of the instability results in peeling off only a thin layer at the crustal base, as the shallower region is too viscous to participate in delamination. Due to its thinness, thermal diffusion can swiftly cool the delaminated region and restore the thermal structure prior to the onset of the instability. Even when the growth timescale of the instability is shorter than a geological time, cooling by thermal diffusion can limit the development of further RT instability, minimizing the likelihood of crustal foundering.

The presence of a dense crust is also likely on Io, where a crust is suggested to be floating on a subsurface magma ocean. Because the solid phase is denser than the melt for silicates, the crust is expected to have greater density than the underlying magma ocean. However, an extreme temperature increase at the crustal base, which is expected for bodies releasing energy through heat pipes, leads to a very small viscosity scale height and can significantly extend the instability timescale. The



extent of delamination will also be limited to the bottom  $<100$  m, and thus thermal diffusion can swiftly cool the delaminated region and recover the initial thermal profile, restoring crustal thickness through the solidification of a magma ocean. As the initial structure is restored, the RT instability is expected to be triggered again, but the crust recovers its thickness after each instability, and this cyclic process maintains the presence of the dense crust over an extended period (Figure 2(A)). Disruptions unrelated to the putative instability, including fractures and impacts, may lead to overturning the dense crust, and such a process cannot be entirely ruled out. Bodies with a low-viscosity mantle (including a subsurface magma ocean), in particular, may be susceptible to overturn by channelized mantle upwelling. Nevertheless, the presented framework of the RT instability underscores the nuanced stability of a dense crust on planetary bodies, offering new insights into the geological evolution of such objects.

### Acknowledgments

This work was motivated by NASA's Juno mission. Y.M. was supported by the Stanback Postdoctoral Fellowship from the Caltech Center for Comparative Planetary Evolution. The authors also thank two anonymous reviewers, whose comments were helpful to improve the clarity of the manuscript.

## Appendix A The Crust–Mantle Density Difference on Io

If Io's crust results from the solidification of erupted melt, the crustal composition can be estimated through the partial melting of the mantle. We utilize the MELTS model (Ghiorso 1994) to predict the density and composition of the partial melt of peridotite at various degrees of melting, and the Theriak-Domino model is employed to determine the density of solidified melt (de Capitani & Petrakakis 2010; Figure 7). Under a low degree of partial melting, as on Earth, a basaltic crust forms, which is less dense than the underlying mantle, and this could be inhibiting subduction in young oceanic

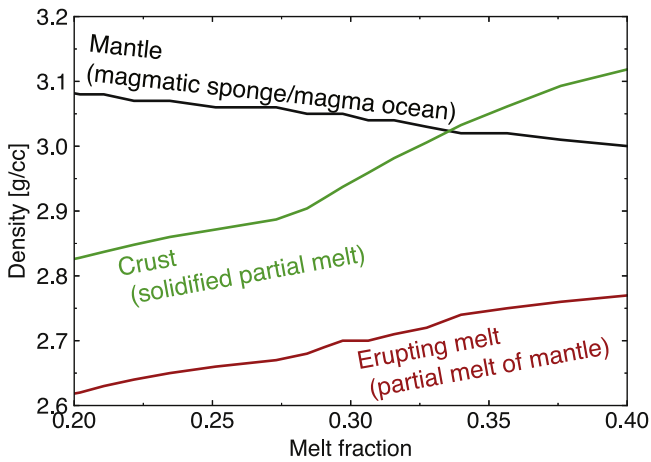


**Figure 7.** Densities of a partially molten mantle (black) and crust (green) are shown as a function of mantle melt fraction. A peridotitic mantle is assumed here, and crust is considered to be formed through the solidification of partial melt (red). Upon solidification, the partial melt becomes denser than the underlying mantle for a melt fraction larger than  $\sim 0.33$ . Partial melt composition is calculated using MELTS (Ghiorso 1994), and the mineral composition and density of the solidified melt are predicted using Theriak-Domino (de Capitani & Petrakakis 2010).

lithosphere. Io, however, probably presents a different situation. With a higher degree of melting, the partial melt becomes more ultramafic, and eventually peridotitic. A crust of higher density is formed as a result, and for a peridotitic mantle the crust becomes denser than the underlying mantle for  $\phi \gtrsim 0.3$  (Figure 7).

In the presence of a subsurface magma ocean, with  $\phi$  exceeding the critical melt fraction for rheological transition ( $\sim 0.4$ ), the crust is expected to be denser than the mantle. Even a very high degree of partial melt (magmatic sponge) may produce a dense crust.

## Appendix B Derivation of Dispersion Relation

### B.1. Rayleigh–Taylor Instability of a Thin Elastic Layer

We consider a system with two elastic layers: a top layer with thickness  $h$  and density  $\rho_1$  overlying one with  $\rho_2 (< \rho_1)$ . The two layers are set to have elasticities of  $\mu_1$  and  $\mu_2$ , respectively, and the viscosity is assumed to be negligible. The derivation of the dispersion relation for viscous layers is delineated in Chandrasekhar (1961) and Conrad & Molnar (1997), so in the following we focus on an elastically behaving system with a finite-thickness upper layer.

The dispersion relation can be derived from the perturbed equations of mass and momentum conservation. We assume that a perturbation of a wavelength  $\lambda$  develops at the interface between the two layers and calculate its growth rate, assuming an exponential growth of perturbation with time ( $\sim e^{\psi t}$ ). This is equivalent to expanding the perturbed variables with various wavenumbers, and we obtain the following ordinary differential equation on the vertical ( $z$ -direction) velocity,  $u_z$ :

$$\begin{aligned} k^2 \left( -\psi^2 \rho_0 + \mu \left( -k^2 + \frac{d^2}{dz^2} \right) + 2 \frac{d\mu}{dz} \frac{d}{dz} + g \frac{d\rho_0}{dz} \right) u_z \\ = \frac{d}{dz} \left( -\psi^2 \rho_0 \frac{d}{dz} + \mu \left( -k^2 + \frac{d^2}{dz^2} \right) \frac{d}{dz} \right. \\ \left. + \frac{d\mu}{dz} \left( \frac{d^2}{dz^2} + k^2 \right) \right) u_z, \end{aligned} \quad (\text{B1})$$

where  $k (=2\pi/\lambda)$  is the wavenumber of horizontal perturbation. It is noted that the displacement,  $\Delta x_i$ , needed to calculate the stress can be described by the integral of velocity:

$$\Delta x_i = \int u_i dt \simeq \frac{u_i}{\psi}. \quad (\text{B2})$$

The general solution of  $u_z$  within the upper layer is

$$\begin{aligned} u_z(z) = A_1 \exp(-kz) + B_1 \exp(kz) \\ + C_1 \exp(-q_1 z) + D_1 \exp(q_1 z), \end{aligned} \quad (\text{B3})$$

where  $q_1 = \sqrt{k^2 + \psi^2 \rho_1 / \mu_1}$ , and that within the lower layer takes a similar form, except that by assuming an infinitely deep layer,  $u_z$  must vanish at  $z \rightarrow -\infty$ :

$$u_z(z) = B_2 \exp(kz) + D_2 \exp(q_2 z), \quad (\text{B4})$$

where  $q_2 = \sqrt{k^2 + \psi^2 \rho_2 / \mu_2}$ .

Equations (B3) and (B4) indicate that six boundary conditions are necessary to derive the dispersion relation. The continuity of velocities and tangential stresses at the interface

between the two layers provide three boundary conditions, and the integration of Equation (B1) across the fluid interface provides another. These four boundary conditions would yield the following dispersion relation when both layers are infinite in thickness (as  $B_1$  and  $D_1$  are negligible):

$$\begin{aligned} & -\left\{\frac{gk}{\psi^2}\left(\frac{\rho_2 - \rho_1}{\rho_1 + \rho_2}\right) + 1\right\}(\rho_1 + \rho_2)(\rho_2 q_1 + \rho_1 q_2 - k) \\ & -4k\rho_1\rho_2 + \frac{4k^2}{\psi^2}(\mu_2 - \mu_1)\{(\rho_1 q_2 - \rho_2 q_1) \\ & + k(\rho_2 - \rho_1)\} + \frac{4k^3}{\psi^4}(\mu_2 - \mu_1)^2(q_1 - k)(q_2 - k) = 0. \end{aligned} \quad (\text{B5})$$

It is noted that, while the equivalent equation for viscous systems always has a root of  $\psi > 0$  (Chandrasekhar 1961), the

atmospheric pressure:

$$\begin{aligned} P' &= \left(P_{\text{atm}} - \frac{\mu_1}{\psi} \frac{\partial u_z}{\partial z}\right) - (P_{\text{atm}} - \rho g \varepsilon) \\ &= \rho g \varepsilon - \frac{\mu_1}{\psi} \frac{\partial u_z}{\partial z}, \end{aligned} \quad (\text{B8})$$

where  $\varepsilon$  is the displacement by deformation at the top boundary ( $z = h$ ). By relating the vertical motion with the displacement ( $u_z|_{z=h+\varepsilon} = \partial \varepsilon / \partial t$ ), we obtain

$$\frac{\partial^3 u_z}{\partial t^2 \partial z} = g \left( \frac{\partial}{\partial x^2} + \frac{\partial}{\partial y^2} \right) u_z + \frac{\mu_1}{\rho_1 \psi} \frac{\partial^4 u_z}{\partial t \partial z^3}. \quad (\text{B9})$$

The general solution of  $u_z$  is solved under these six boundary conditions. These two conditions, together with the four boundary conditions at  $z = 0$ , can be written in a matrix form:

$$\begin{pmatrix} 1 & 1 & 1 & 1 & -1 & -1 \\ k & -k & q_1 & -q_1 & k & q_2 \\ 2\mu_1 k^2 & 2\mu_1 k^2 & \mu_1(k^2 + q_1^2) & \mu_1(k^2 + q_1^2) & -2\mu_2 k^2 & -\mu_2(k^2 + q_2^2) \\ \frac{1}{2}R - C - \rho_1 & \frac{1}{2}R + C + \rho_1 & \frac{1}{2}R - \frac{q_1}{k}C & \frac{1}{2}R + \frac{q_1}{k}C & \frac{1}{2}R + C - \rho_2 & \frac{1}{2}R + \frac{q_2}{k}C \\ 2k^2 e^{-kh} & 2k^2 e^{kh} & (k^2 + q_1^2)e^{-q_1 h} & (k^2 + q_1^2)e^{q_1 h} & 0 & 0 \\ W & X & Y & Z & 0 & 0 \end{pmatrix} \begin{pmatrix} A_1 \\ B_1 \\ C_1 \\ D_1 \\ A_2 \\ B_2 \end{pmatrix} = 0, \quad (\text{B10})$$

one for elastic systems does not have a real root of  $\psi$  for wavelengths shorter than a critical value  $\lambda_c$  (Equation (18)).

For a system with a finite-thickness upper layer, two additional boundary conditions are necessary at the upper side of a crustal layer (Kaus & Becker 2007). The upper side of the crust is not bounded by anything and can move freely, but as tangential stress cannot be supported by a vacuum,  $\sigma_{xz}$  and  $\sigma_{yz}$  must be zero at the top boundary ( $z = h$ ):

$$\begin{aligned} \sigma_{xz} &= \frac{\mu_1}{\psi} \left( \frac{\partial u_x}{\partial z} + \frac{\partial u_z}{\partial x} \right) = 0, \\ \sigma_{yz} &= \frac{\mu_1}{\psi} \left( \frac{\partial u_y}{\partial z} + \frac{\partial u_z}{\partial y} \right) = 0, \end{aligned} \quad (\text{B6})$$

thus

$$\left( -\frac{\partial^2}{\partial x^2} - \frac{\partial^2}{\partial y^2} + \frac{\partial^2}{\partial z^2} \right) u_z = \left( k^2 + \frac{\partial^2}{\partial z^2} \right) u_z = 0. \quad (\text{B7})$$

Also, similar to the case of ocean surface waves, pressure at the deformed top boundary should adjust to balance the

where

$$W = \left( -k\psi^2 + gk^2 + \frac{\mu_1}{\rho_1} k^3 \right) e^{-kh}, \quad (\text{B11})$$

$$X = \left( k\psi^2 + gk^2 - \frac{\mu_1}{\rho_1} k^3 \right) e^{kh}, \quad (\text{B12})$$

$$Y = \left( -q_1\psi^2 + gk^2 + \frac{\mu_1}{\rho_1} q_1^3 \right) e^{-q_1 h}, \quad (\text{B13})$$

and

$$Z = \left( q_1\psi^2 + gk^2 - \frac{\mu_1}{\rho_1} q_1^3 \right) e^{q_1 h}. \quad (\text{B14})$$

Conditions where the determinant is nonzero are solved and plotted in Figure 8.

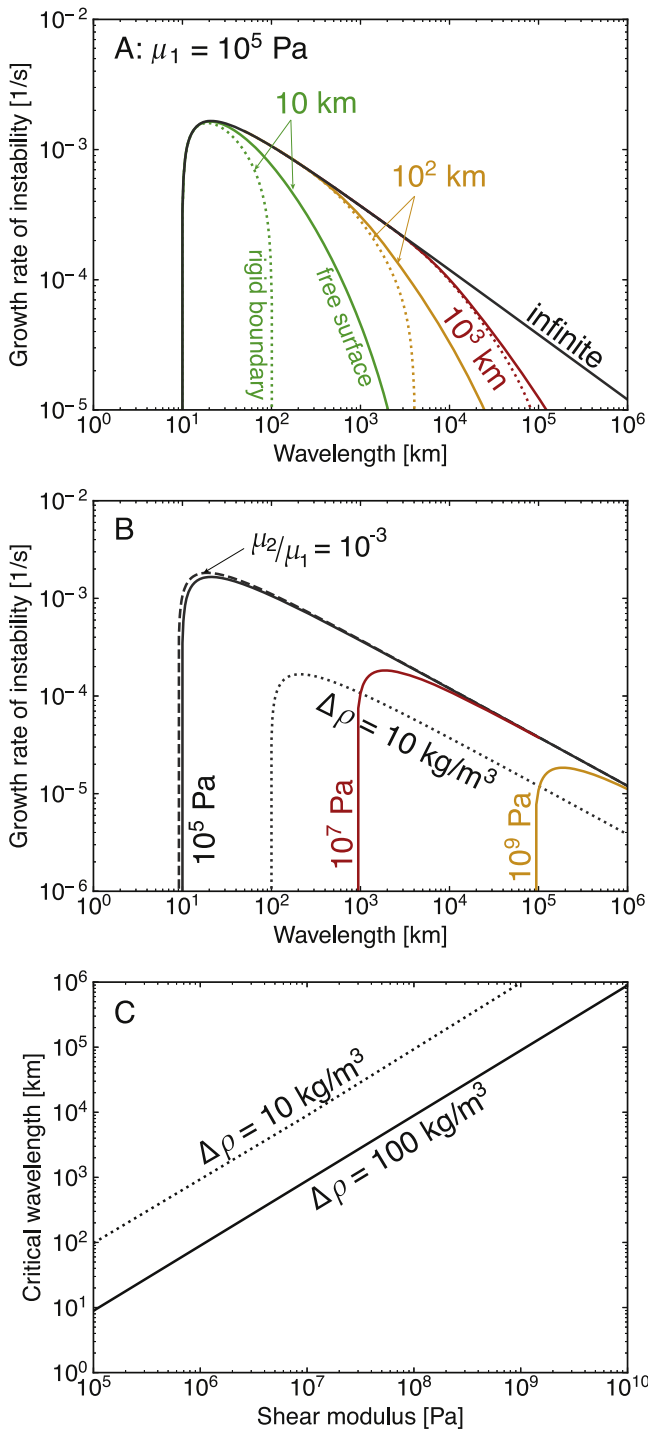


**Figure 8.** (A), (B) Dispersion relations of the RT instability for a denser elastic layer overlying a lighter one. (A) Colors indicate different layer thicknesses (10 km, green;  $10^2$  km, orange;  $10^3$  km, red), and the black line corresponds to when both layers are infinitely thick (Terrones 2005). Shear moduli of  $10^5$  and  $10^4$  Pa are assumed for the upper and lower layers, respectively, and the density difference is set to  $\Delta\rho = 100$  kg m<sup>-3</sup>. For results with finite-thickness, rigid boundary conditions (dotted) and free surface (solid) are assumed, but the maximum growth rates show little difference between the two conditions. (B) The same as (A) but varying the values of  $\mu_1$  ( $10^5$  Pa, black;  $10^7$  Pa, red;  $10^9$  Pa, orange). The results for  $\Delta\rho = 10$  kg m<sup>-3</sup> (dotted) and  $\mu_2 = 10^2$  Pa (dashed) are also plotted. (C) The minimum (critical) wavelength to induce the RT instability as a function of  $\mu_1$ . Two values of  $\Delta\rho$  (10, dotted; 100 kg m<sup>-3</sup>, solid) are shown.

## ORCID iDs

Yoshinori Miyazaki <https://orcid.org/0000-0001-8325-8549>  
David J. Stevenson <https://orcid.org/0000-0001-9432-7159>

## References

- Anderson, J. D., Lau, E. L., Sjogren, W. L., Schubert, G., & Moore, W. B. 1996a, *Natur*, **384**, 541
- Anderson, J. D., Sjogren, W. L., & Schubert, G. 1996b, *Sci*, **272**, 709
- Andersson, O., & Inaba, A. 2005, *PCCP*, **7**, 1441
- Barr, A. C., & McKinnon, W. B. 2007, *JGRE*, **112**, E02012
- Biersen, C., & Nimmo, F. 2016, *JGRE*, **121**, 2211
- Bills, B. G., & Nimmo, F. 2008, *Icar*, **196**, 293
- Bjornnes, E., Johnson, B. C., Silber, E. A., Singer, K. N., & Evans, A. J. 2022, *JGRE*, **127**, e2021JE007028
- Bland, M. T., Showman, A. P., & Tobie, G. 2009, *Icar*, **200**, 207
- Brown, S., Zhang, Z., Bolton, S., et al. 2023, *JGRE*, **128**, e2022JE007609
- Cassen, P., Reynolds, R. T., & Peale, S. J. 1979, *GeoRL*, **6**, 731
- Castillo-Rogez, J. C., Efroimsky, M., & Lainey, V. 2011, *JGRE*, **116**, E09008
- Chandrasekhar, S. 1961, *Hydrodynamic and Hydromagnetic Stability*, International Ser. of Monographs on Physics (Oxford: Oxford Univ. Press)
- Conrad, C. P., & Molnar, P. 1997, *GeoJI*, **129**, 95
- Croft, S. K. 1980, *LPSC*, **11**, 2347
- Davaille, A., & Jaupart, C. 1994, *JGR*, **99**, 19853
- de Capitani, C., & Petrakakis, K. 2010, *AmMin*, **95**, 1006
- De La Chapelle, S., Castelnau, O., Lipenkova, V., & Duval, P. 1998, *JGR*, **103**, 5091
- Dumoulin, C., Doin, M. P., & Fleitout, L. 1999, *JGR*, **104**, 12759
- Durham, W., Prieto-Ballesteros, O., Goldsby, D. L., & Kargel, J. 2010, *SSRv*, **153**, 273
- Faul, U. H., & Jackson, I. 2005, *E&PSL*, **234**, 119
- Gammon, P. H., Kieft, H., Clouter, M. J., & Denner, W. W. 1983, *JGlac*, **29**, 433
- Gerya, T. V., Stern, R. J., Baes, M., Sobolev, S. V., & Whattam, S. A. 2015, *Natur*, **527**, 221
- Ghiorso, M. S. 1994, *GeCoA*, **58**, 5489
- Goldsby, D. L., & Kohlstedt, D. L. 2001, *JGRB*, **106**, 11017
- Greeley, R., Klemaszewski, J. E., Wagner, R., & Team, t. G. I. 2000, *P&SS*, **48**, 829
- Greenberg, R., Geissler, P., Hoppa, G., & Tufts, B. R. 2002, *RvGeo*, **40**, 1
- Hager, B. H., & O'Connell, R. J. 1981, *JGR*, **86**, 4843
- Hesse, M. A., & Castillo-Rogez, J. C. 2019, *GeoRL*, **46**, 1213
- Hirth, G., & Kohlstedt, D. L. 1996, *E&PSL*, **144**, 93
- Jackson, I., Faul, U. H., Fitz Gerald, J. D., & Tan, B. H. 2004, *JGRB*, **109**, B06201
- Jain, C., Korenaga, J., & Karato, S. I. 2018, *JGRB*, **123**, 674
- Jain, C., Korenaga, J., & Karato, S. I. 2019, *JGRB*, **124**, 310
- Katz, R. F., Spiegelman, M., & Langmuir, C. H. 2003, *GGG*, **4**, 1073
- Kaus, B. J., & Becker, T. W. 2007, *GeoJI*, **168**, 843
- Keane, J. T., Matsuyama, I., Biersen, C. J., & Trinh, A. 2023, in *Tidal Heating and the Interior Structure of Io, Io: A New View of Jupiter's Moon*, Astrophysics and Space Science Library, Vol. 468, ed. R. M. C. Lopes, K. de Kleer, & J. T. Keane (Berlin: Springer), 95
- Kemp, D. V., & Stevenson, D. J. 1996, *GeoJI*, **125**, 73
- Khurana, K. K., Jia, X., & Kivelson, M. G. 2011, *Sci*, **332**, 1186
- Kirchoff, M. R., & McKinnon, W. B. 2009, *Icar*, **201**, 598
- Kirk, R. L., & Stevenson, D. J. 1987, *Icar*, **69**, 91
- Love, A. E. H. 1909, *RSPSA*, **82**, 73
- Mankovich, C. R., & Fuller, J. 2021, *NatAs*, **5**, 1103
- Matsuyama, I., Keane, J., Trinh, A., Beuthe, M., & Watters, T. R. 2021, *Icar*, **358**, 114202
- McCarthy, C., & Castillo-Rogez, J. C. 2013, in *The Science of Solar System Ices*, Astrophysics and Space Science Library, Vol. 356, ed. M. Gudipati & J. C. Castillo-Rogez (Berlin: Springer), 183
- McGovern, P. J., Kirchoff, M. R., White, O. L., & Schenk, P. M. 2016, *Icar*, **272**, 246
- McKinnon, W. B. 2006, *Icar*, **183**, 435
- McKinnon, W. B., Schenk, P. M., & Dombard, A. J. 2001, *Geo*, **29**, 103
- Mei, S., Bai, W., Hiraga, T., & Kohlstedt, D. L. 2002, *E&PSL*, **201**, 491
- Mei, S., & Kohlstedt, D. L. 2000, *JGR*, **105**, 457

- Mei, S., Suzuki, A. M., Kohlstedt, D. L., Dixon, N. A., & Durham, W. B. 2010, [JGRB](#), **115**, B08204
- Miyazaki, Y., & Stevenson, D. J. 2022, [PSJ](#), **3**, 256
- Molnar, P., Houseman, G. A., & Conrad, C. P. 1998, [GeoJI](#), **133**, 568
- Mondal, P., & Korenaga, J. 2018, [GeoJI](#), **212**, 1890
- Nagel, K., Breuer, D., & Spohn, T. 2004, [Icar](#), **169**, 402
- Nimmo, F. 2004, in Workshop on Europa's Icy Shell: Past, Present, and Future (Houston, TX: Lunar and Planetary Inst.), 7005
- Nimmo, F., & Gaidos, E. 2002, [JGR](#), **107**, E45021
- Nimmo, F., Pappalardo, R. T., & Giese, B. 2002, [GeoRL](#), **29**, 1158
- O'Neill, C., Marchi, S., Zhang, S., & Bottke, W. 2017, [NatGe](#), **10**, 793
- O'Reilly, T. C., & Davies, G. F. 1981, [GeoRL](#), **8**, 313
- Park, R. S., Konopliv, A. S., Bills, B. G., et al. 2016, [Natur](#), **537**, 515
- Parmentier, E. M., & Head, J. W. 1981, [Icar](#), **47**, 100
- Parmentier, E. M., Squyres, S. W., Head, J. W., & Allison, M. L. 1982, [Natur](#), **295**, 290
- Peale, S. J., Cassen, P. M., & Reynolds, R. T. 1979, [Sci](#), **203**, 892
- Qi, C., Stern, L. A., Pathare, A., Durham, W. B., & Goldsby, D. L. 2018, [GeoRL](#), **45**, 12757
- Renaud, J. P., & Henning, W. G. 2018, [ApJ](#), **857**, 98
- Roberts, J. H., Lillis, R. J., & Manga, M. 2009, [JGRE](#), **114**, E04009
- Rubin, M. E., Desch, S. J., & Neveu, M. 2014, [Icar](#), **236**, 122
- Sasaki, T., & Abe, Y. 2007, [EP&S](#), **59**, 1035
- Schubert, G., Anderson, J. D., Spohn, T., & McKinnon, W. B. 2004, in Jupiter: The Planet, Satellites and Magnetosphere, ed. F. Bagenal, T. E. Dowling, & W. B. McKinnon (Cambridge: Cambridge Univ. Press), 281
- Shoemaker, E. M., Lucchitta, B. K., Wilhelms, D. E., Plescia, J. B., & Squyres, S. W. 1982, in Satellites of Jupiter, ed. D. Morrison (Tucson, AZ: Univ. Arizona Press), 435
- Shoji, D., Hussmann, H., Kurita, K., & Sohl, F. 2013, [Icar](#), **226**, 10
- Shoji, D., & Kurita, K. 2014, [JGRE](#), **119**, 2457
- Spencer, D. C., Katz, R. F., & Hewitt, I. J. 2020, [JGRE](#), **125**, e2020JE006443
- Spencer, J. R. 1987, [Icar](#), **70**, 99
- Stein, N., Ehlmann, B. L., Stevenson, D. J., Castillo-Rogez, J., & Raymond, C. A. 2023, [JGRE](#), **128**, e2023JE007868
- Stevenson, D. J. 1990, in Core Formation, Origin of the Earth, ed. H. Newsom & J. E. Jones (Oxford: Oxford Univ. Press), 231
- Terrones, G. 2005, [PhRvE](#), **71**, 036306
- Terrones, G., & Carrara, M. D. 2015, [PhFI](#), **27**, 054105
- Turcotte, D. L., & Schubert, G. 2002, Geodynamics (2nd ed.; Cambridge: Cambridge Univ. Press)
- Vance, S., Bouffard, M., Choukroun, M., & Sotin, C. 2014, [P&SS](#), **96**, 62
- Veeder, G. J., Davies, A. G., & Matson, D. L. 2012, [Icar](#), **219**, 701
- Wahl, S. M., Hubbard, W. B., Militzer, B., et al. 2017, [GeoRL](#), **44**, 4649
- Watters, W. A., Zuber, M. T., & Hager, B. H. 2009, [JGRE](#), **114**, E02001
- Zahnle, K., Schenk, P., Levison, H., & Dones, L. 2003, [Icar](#), **163**, 263